frontiers | Frontiers in Earth Science

TYPE Original Research
PUBLISHED 27 December 2023
DOI 10.3389/feart.2023.1289000



OPEN ACCESS

EDITED BY
Alcides Nobrega Sial,
Federal University of Pernambuco, Brazil

REVIEWED BY
Miguel Parada,
University of Chile, Chile
Liang Qiu,
China University of Geosciences, China

*CORRESPONDENCE
Xiao-Feng Qin,
qxf@glut.edu.cn

RECEIVED 05 September 2023
ACCEPTED 03 November 2023
PUBLISHED 27 December 2023

CITATION
Li D-R, Hu G-A, Qin X-F, Zhao Y-L, Mo H and He W-L (2023), Petrogenesis and metallogenic significance of late Mesozoic granites in the Akjilga mining area, Tajikistan: constraints from geochronology and geochemistry. *Front. Earth Sci.* 11:1289000. doi: 10.3389/feart.2023.1289000



# Petrogenesis and metallogenic significance of late Mesozoic granites in the Akjilga mining area, Tajikistan: constraints from geochronology and geochemistry

Dong-Ren Li[1,2], Gui-Ang Hu[3], Xiao-Feng Qin[1,2]*, Yu-Lei Zhao[1], Hui Mo[3] and Wen-Lu He[3]

[1]College of Earth Science, Guilin University of Technology, Guilin, China, [2]Guangxi Key Laboratory of Hidden Metal Mineral Exploration, Guilin University of Technology, Guilin, China, [3]Guangxi Nonferrous Metals Group Resources Exploration Co., Ltd., Nanning, China

The Akjilga (Акджилга) mining area in Tajikistan sits in the central part of the Pamir syntaxis in the western part of the Indo–Eurasia collisional orogenic belt. Recently, the mineralization phenomena of skarn-type tin polymetallic ore bodies and dolomite-type rare-earth metals in the copper polymetallic mining area have been reported. However, the limited knowledge on the genesis of granite and its relationship with mineralization in this area hinders further research. Here, the Late Mesozoic granite rocks in the mining area were studied by petrology, geochemistry, and zircon U–Pb dating. The results showed that the rocks comprise majorly porphyric biotite syenogranite and minorly porphyric biotite monzogranite. The zircon U–Pb age of the porphyric biotite syenogranite was 108.3 ± 2.0 Ma, highlighting the Early Cretaceous period. The porphyric biotite syenogranite features high silicon and potassium contents and low iron, magnesium, calcium, sodium, titanium, and phosphorus contents. Furthermore, their aluminum saturation indexes were 1.11–1.21. Therefore, they were classified as high-potassium calc-alkaline strong peraluminous rocks. Trace-element analysis showed the enrichment of large ionic lithophile elements and light rare-earth elements (REEs); the deficiency of high-field-strength elements and heavy REEs; and the negative anomalies of Nb, P, and Ti. Compared with ordinary granites, the porphyric biotite syenogranite exhibits a higher differentiation index (91.20–93.96) and strong negative Eu anomaly (0.05–0.26), as well as a low Zr content and abnormally low Nb/Ta, Zr/Hf, Y/Ho, ∑LREE/∑HREE ratios. Therefore, the rocks are considered highly differentiated I-type granites with good Sn polymetallic and rare-metal prospecting potentials, and it resulted in the subduction-collision of the Rushan-Pshart ocean between the Middle Pamir block and the South Pamir block during the northward subduction process of the Late Mesozoic New Tethys ocean (Shyok ocean).

KEYWORDS

**zircon U-Pb chronology, geochemistry, late mesozoic granite, Akjilga mining area, Tajikistan**

# 1 Introduction

Located in the hinterland of Central Asia, Tajikistan sits amidst two tectonic domains of Ancient Asia and Tethys, at the intersection of several orogenic belts (e.g., Tianshan, West Kunlun, Karakoram, Pamir, and the Hindu Kush in the northwest of the Qinghai–Tibet Plateau), and at the western arc of the Himalayan arc orogenic belt. Therefore, it is called the "western syntaxis" by the geologists (Fan et al., 2017; 2020; 2022; Bai et al., 2019; Zhang et al., 2019; Wang et al., 2020; Zhang et al., 2022). Since the Late Neoproterozoic period, the region has experienced long-term continental fragmentation, closure of the ancient Tethys ocean, and continental crust proliferation (Burtman and Molnar, 1993; Yin and Harrison, 2000; Xiao et al., 2002; Robinson et al., 2004; 2007; Cao et al., 2015; Cai et al., 2016; Cao et al., 2018). Additionally, since the Cenozoic period, the region has experienced the superimposed transformation of subduction and collision, as well as the tectonic uplift of the Indo–Eurasian plate (Burtman and Molnar, 1993; Burtman, 2000; Robinson et al., 2004; 2007; Sobel et al., 2013; Stübner et al., 2013a; Cao et al., 2015; Rutte et al., 2017a; Cao et al., 2018). Consequently, the tectonic–magmatic evolution and mineralization processes in this area are long and intense; the tectonic processes are complex and diverse; compound mineralization is prominent, explaining the extremely complex structural features and magmatic rock associations of different ages and lithologies; and the various metal mineral resources related to magmatism are abundant (Fan et al., 2017; Fan et al., 2020; Fan et al., 2022; Zhang et al., 2022).

Among them, the Paleo–Asian tectonic domain in Northern Tajikistan has been extensively researched and features more than 400 gold, copper, silver, antimony, mercury, lead, zinc, tungsten, tin, uranium, and other deposits (points) (Li et al., 2013; Fan et al., 2017; 2020; Cheng et al., 2022). In particular, the Zeravshan gold–rare metal metallogenic belt is the most important metallogenic belt in Tajikistan. Six large gold deposits have been discovered in the zone, For example, Tarot (Тарор), gelato (Джилао), Chore (цоре), East Duoba (Восточная Дуоба), Uchkol (Учколь) and Upper Kumarg Верчний КумарГ). It is one of the largest gold concentration areas in Central Asia, with 3 medium gold deposits in Gizhdarva, Shahbas, and Kum-Mano, as well as over 110 small gold deposits (*in situ*) (Sui, 2010; Li et al., 2013; Yang et al., 2013; Fan et al., 2017; 2020; Sui, 2018). Therefore, Northern Tajikistan is an important part of the world-class gold metallogenic belt known as the "gold belt of Central Asia" (Tu, 1999; Xue et al., 2014a; Zhang H. S. et al., 2016; Li and Zhou, 2019; Cheng et al., 2022). The Tethys tectonic domain in the south of Tajikistan, due to its geographical position in the Pamir Plateau, belongs to the central part of the "western syntaxis" The zonal and meridional mountains are intertwined, the terrain is extremely complex, the average altitude is up to 5,000 m, and the main peaks are more than 6,000–7,000 m high (Wang et al., 2020). Therefore, this area is rarely visited because the natural geographical environment is extremely unfriendly, transportation is inconvenient, and the geological work was mainly completed under the former Soviet Union. Furthermore, the volume of geological mineral studies is low, particularly in the case of the South Pamir region where the known minerals are limited to those found in a few deposits (points) under the former Soviet Union (Fan et al., 2017; Zhang et al., 2019; Wang et al., 2020). Moreover, the information on the diagenetic age, tectonic environment, and metallogenic specificity of the magmatic rocks developed widely in this area is controversial, and there is a lack of a unified understanding and systematic research (Schwab et al., 2004; Stübner et al., 2013a; b; Fan et al., 2017; 2020; 2022; Cheng et al., 2022; Zhang et al., 2022).

Recently, several iron–copper polymetallic mineralizations have been discovered in the South Pamir region of Tajikistan (Zhang G. Z. et al., 2016). Large and super-large lithium deposits, such as Pasgusta and Jamanak, have been discovered in the Hindu Kush region to the west, and pegmatitic lithium deposits with large and super-large prospects, such as Dahongliutan and Capagou, have also been found in the West Kunlun region of China to the east (Wang, 2016). In the South Pamir region of central Tajikistan, due to the low quantity of early works, no lithium deposit has been found, although numerous similar magmatic rocks have developed in this area. Some geologists believe that this area might be a world-class "lithium belt" (Fan et al., 2022). In recent years, during the detailed investigation of the Akjilga copper polymetallic deposit in the South Pamir region of Tajikistan, the tin polymetallic ore body was first discovered in the contact zone between Mesozoic granite and the surrounding rock. This indicates that this area and its adjacent areas have great prospecting potential for nonferrous metals and rare metals. In this study, the field geology, petrography, geochemistry, and zircon U–Pb chronology of the Mesozoic granites in the Akjilga copper polymetallic deposit are systematically examined. Furthermore, the petrogenesis and the relationship between the granites and mineralization are discussed to provide a petrological basis for the study of the relationship between diagenesis and mineralization and for geological prospecting in this area.

# 2 Geological background and characteristics of granitic pluton

The study area is located in the central part of the "western syntaxis" (also known as the "Pamir syntaxis") of the western segment of the Indo–Eurasia collisional orogenic belt, which is bounded by the Shyok suture zone to the south and the main Pamir thrust fault zone to the north (Figure 1A). Based on the ophiolite belt, magmatic rock features, and sedimentary construction characteristics, the Pamir syntaxis is further divided into three blocks: North Pamir, Middle Pamir and South Pamir. Further, the interiors are separated by the Tanymas suture zone and the Rushan–Pshart suture zone, respectively (Figure 1A) (Burtman and Molnar, 1993; Burtman, 2000; Robinson et al., 2004; 2007; Schneider et al., 2013; Zhang et al., 2019; Liu et al., 2020; Ma et al., 2022; Zhang et al., 2022). The North Pamir block, which is connected to the Kunlun orogenic belt in China, mainly features two sets of rock units: the Early Paleozoic accretionary complex and the main thrust sheet system originating from the Mesozoic period. The magmatic rocks comprise mainly Early Paleozoic volcanic rocks and granitic intrusive rocks, as well as the Late Triassic–Early Jurassic island arc-type granites (Robinson, 2015; Zhang et al., 2018; Imrecke et al., 2019; Zhang et al., 2022). The Central Pamir block is connected to the Songpan–Ganzi block, and its mainly feature is amphibolite facies metamorphic Ediacaran basement rocks with strong deformation, as well as Late

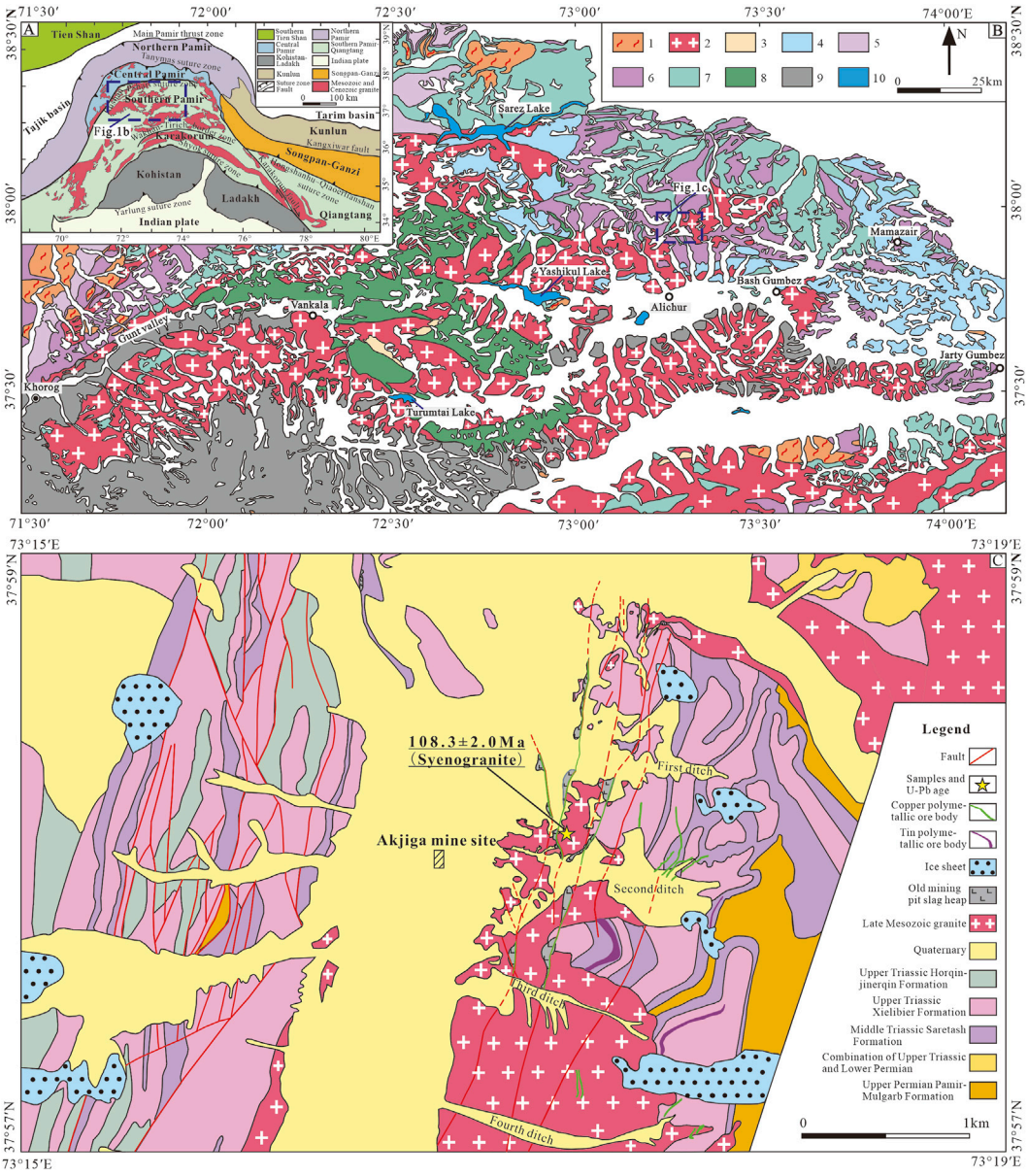


FIGURE 1
**(A)** Simplified tectonic map of the Pamir region (modified after Stübner et al., 2013a, b; Zhang et al., 2019; Ma et al., 2022). **(B)** Geological sketch map of the South Pamir region, Tajikistan (modified after Stübner et al., 2013a). **(C)** Geologic map of the Akjilga copper polymetallic metallogenic district, Tajikistan. Figure 1B: 1-Cenozoic (mostly Paleogene) magmatic and volcanoclastic rocks; 2-Pre-Cenozoic (mostly Cretaceous) magmatic rocks; 3-Paleogene-Neogene conglomerate and sandstone; 4-Late Jurassic, above Cimmerian unconformity; 5-Late Triassic-Middle Jurassic; 6-Triassic, below Cimmerian unconformity; 7-Ordovician-Permian; 8-Proterozoic crystalline rocks; 9-Pre-Proterozoic metamorphic rocks; 10-Lake.

Paleozoic and Early Mesozoic flysch sedimentary rocks. Apart from the Mesozoic island arc-type granite, numerous Miocene intrusive rocks are exposed (Ducea et al., 2003; Hacker et al., 2005; Zhang et al., 2022). The South Pamir block and the Karakorum block in the south are generally considered continuous, although separated by the Wakhan–Tirich boundary belt. Together, they form the South Pamir–Karakorum block and are connected to the Qiangtang block in the east (Figure 1A) (Zanchi et al., 2000; Robinson, 2015; Liu et al., 2020; Zhang et al., 2022). The South Pamir block, bounded by the Alichur shear zone, can be further divided into two subtectonic units: southwest Pamir and southeast Pamir. 1) The Precambrian basement strata are mainly developed in southwest Pamir, where the main rock assemblage of the pre-Proterozoic metamorphic rocks is gneiss + migmatite + granulite + quartzite + marble + amphibolite and the main assemblage of the Proterozoic crystalline rocks is gneiss + migmatite + marble. Further, the sedimentary assemblage of carboniferous Permian shale + quartz sandstone is developed in the northern region. 2) Southeast Pamir is dominated by Early Paleozoic and Mesozoic strata: the Ordovician–Lower Permian is mainly flysch-like formation, composed of terrigenous clastic rocks; the Middle Permian–Triassic can be divided into two sets of sedimentary assemblages (carbonate platform and slope-basin

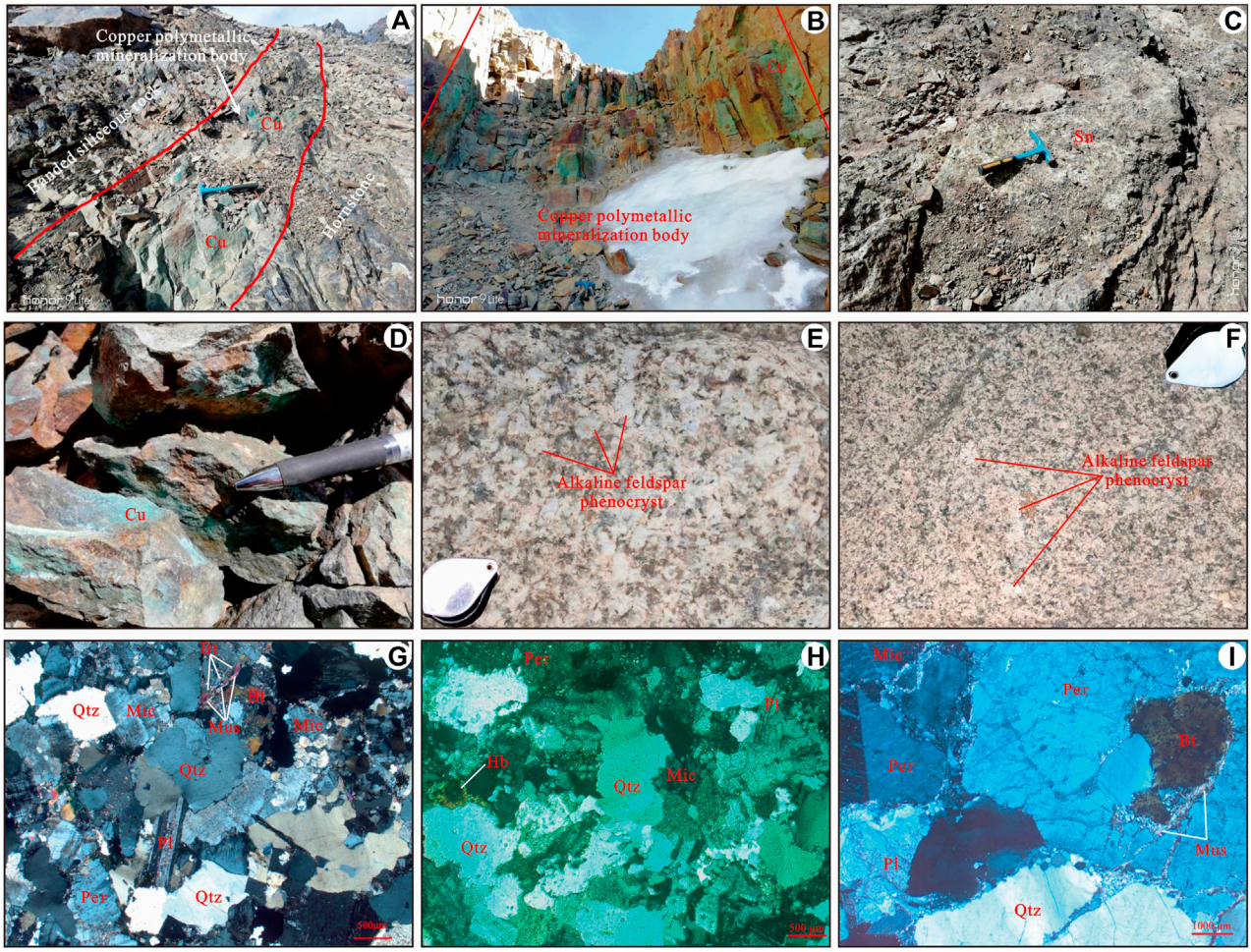


FIGURE 2
**(A)** Copper polymetallic mineralized bodies in fault structural alteration zone. **(B)** Copper polymetallic mineralized bodies in jointed structural alteration zone. **(C)** Tin-bearing skarn. **(D)** Copper-bearing skarn. **(E)** Field Photograph of medium-grained porphyritic granite. **(F)** Field Photograph of fine-grained porphyritic granite. **(G–I)** Micrographs of late Mesozoic granite. Pl-plagioclase; Mic-microcline; Per-perthite; Qtz-quartz; Bt-biotite; Mus-muscovite; Hb-hornblende; Sn-tin; Cu-copper.

sedimentary assemblages); and the Jurassic is dominated by marine limestone deposits, which are in angular unconformity with the lower strata (Figure 1B) (Stübner et al., 2013a; b; Zhang et al., 2019). The most significant feature of the South Pamir block is the large area of pre-Cenozoic (mainly Cretaceous) magmatic rocks and small amounts of Cenozoic (mainly Paleogene) magmatic and pyroclastic rocks (Figure 1B) (Schwab et al., 2004; Malz et al., 2012; Stübner et al., 2013a; b; Aminov et al., 2017; Chapman et al., 2018; Zhang et al., 2019; Zhang et al., 2022).

The Akjilga copper polymetallic deposit examined in this study is located to the north of Alichur, Khorog City, Gorno-Badakhshan Autonomous region, the Republic of Tajikistan, and it is tectonically located in the central and northern parts of the South Pamir block (Figure 1). The strata developed in the mining area comprise mainly Upper Permian, Triassic, and Quaternary. The Upper Permian mainly comprises sandstone and shale, whereas the Triassic mainly comprises a set of carbonate formations interspersed with sandstone and siliceous rocks. The structure is dominated by the near-NS–NE trending fault structure, with noticeable Late Mesozoic granite dislocation phenomena (Figure 1C). The minerals in the mining area are mainly of two types: structurally altered rock-type copper polymetallic ore and skarn-type tin polymetallic ore (Figure 1C). 1) The copper polymetallic ore bodies of the tectonically altered rock type are produced in the near north–south fault structure or the segmented zone (Figures 2A, B). At present, eight ore bodies have been discovered, and the contents of their constituent Cu and Ag elements are 0.4%–7.6% and 0.008%–1.5%, respectively. 2) The skarn-type tin polymetallic ore is a newly discovered ore body, mainly produced in the skarn belt developed between the Late Mesozoic granite and the surrounding rock. From the contact surface between the Late Mesozoic granite and the surrounding rock, tremolite garnet skarn → garnite-bearing tremolite skarn → actinite-bearing tremolite skarn appears successively, with tin and copper mineralizations occurring in the tremolite garnet skarn (Figures 2C, D). The mineralization of copper and zinc occurs in the garnet-bearing tremolite skarn and actinite-bearing tremolite skarn. At present, three tin polymetallic ore bodies have been preliminarily controlled, and the contents of Sn and Cu are 0.4–1.98 wt% and 0.3–5.61 wt%, respectively. The scale of the tin mine is expected to be large (Mo et al., 2019; Liu et al., 2021). In

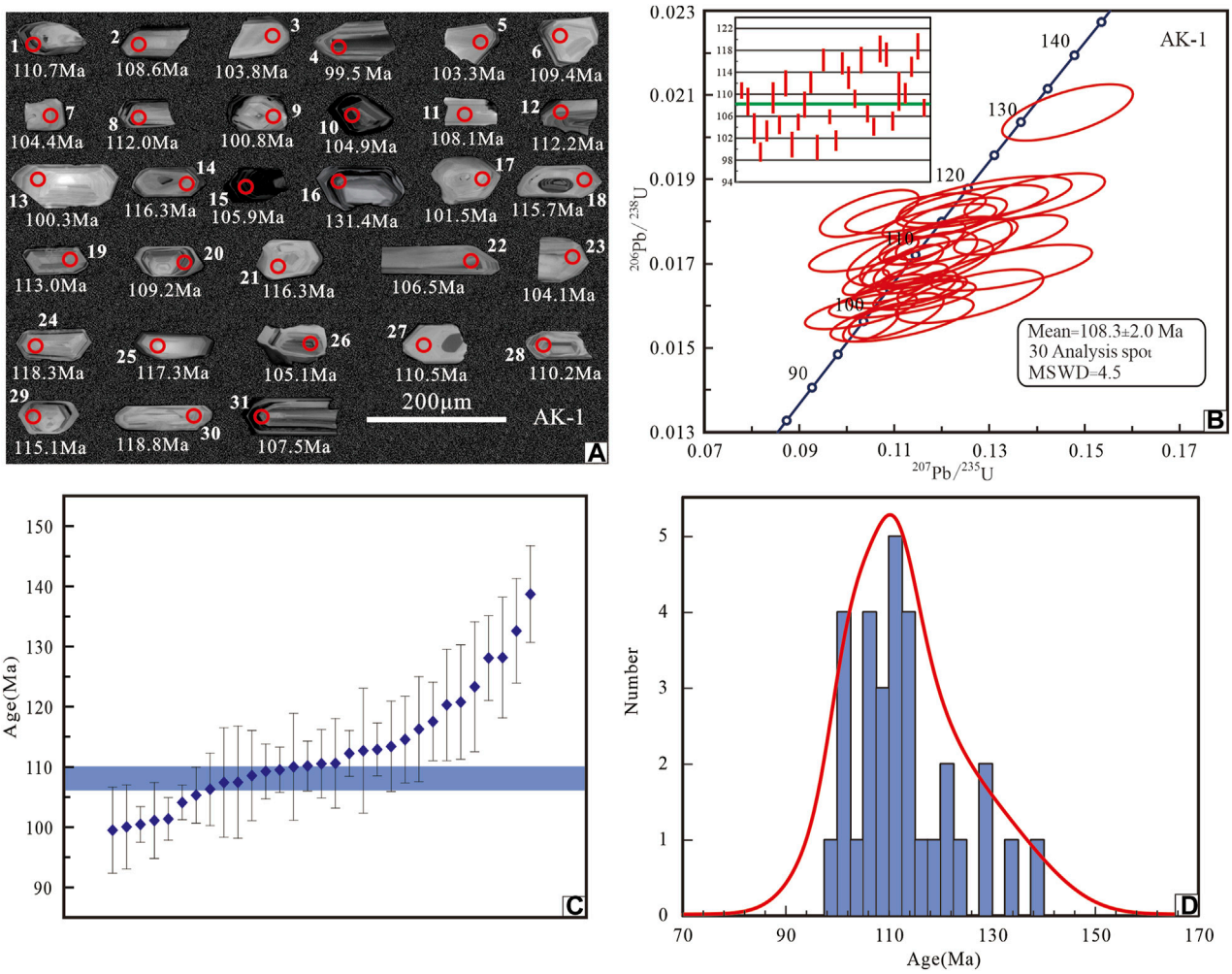


FIGURE 3
**(A)** Zircon Cathodoluminescence (CL) images. **(B)** LA-ICP-MS zircon U-Pb age concordia diagram, with their respective weighted. **(C)** Dates of individual zircon grains of the porphyric biotite syenogranite (AK-1). Blue rectangle represents the weighted average age of the porphyric biotite syenogranite (AK-1). **(D)** Probability density plot of LA-ICP-MS zircon U-Pb age.

addition, the dolomitization zone for the Late Mesozoic granites contains a high content of rare metals, and the contents of Rb, Nb, Ta, Hf, and Zr are 0.036–0.124 wt%, 0.22–0.45 wt%, 0.006–0.112 wt %, 0.007–0.009 wt% and 0.006–0.011 wt%, respectively. Some rocks feature rare-metal minerals of the boundary grade or the lowest industrial grade, indicating that the area also has a good prospecting potential for rare metals.

The Late Mesozoic granitic pluton are mainly distributed in the eastern part of the Akjilga copper polymetallic metallogenic district, and the granitic pluton generally develop in the form of rock branches in the NE–SW direction (Figure 1C). The granitic pluton is in intrusive contact with the Permian–Triassic carbonate rock and clastic rock, the contact surface is smooth-out waveforms, and the cleavage of the surrounding rock is cut off. The surrounding rocks of the outer contact zone exhibit strong contact–thermal metamorphism and metasomatism metamorphism, forming a keratinized zone–skarn zone that is approximately 50–1,600 m wide. The rock types of Late Mesozoic granitic pluton are dominated by porphyric biotite syenogranite, with minorly porphyric biotite monzogranite. The rock has a blocky and porphyritic structure, and the matrix has a medium to fine grained granite structure (Figures 2E, F). The content of phenocrysts are 5–20 vol% (average = 10 vol%), the distribution of phenocrysts are not uniform, and alkaline feldspar phenocryst is the most abundant component, followed by quartz phenocryst and plagioclase phenocryst. Feldspar phenocrysts generally present more idiomorphic columnar shape, with a size of 0.5–1.5 cm (Figures 2E, F). The quartz phenocrysts are irregular in shape and 0.5–0.9 cm in size. The matrix is composed of large amounts of alkaline feldspar (14–38 vol %), plagioclase (16–31 vol%), and quartz (30–48 vol%) and small amounts of biotite (1–8 vol%) (Figure 2G). Occasionally, small amounts of hornblende are found in the local rocks (<2 vol%) (Figure 2H). Alkaline feldspar mainly consists of Microcline, some of which are perthite, in a semi idiomorphic- Irregular shape, with some crystals of alkaline feldspar exhibiting soil like phenomena on their surfaces (Figures 2G, H). Quartz is unevenly distributed in the form of irregular-shaped grains. Hornblende are only occasionally seen in the rocks, and they have mostly undergone strong alteration, sporadically distributed as pseudocrystal in the rocks (Figure 2H). Biotite is in the

**TABLE 1** LA-ICP-MS zircon U-Pb data of porphyric biotite syenogranite in late Mesozoic granitic pluton.

| Spot | Pb | $^{238}$U | $^{232}$Th | Th/U | $^{207}$Pb/$^{206}$Pb | | $^{207}$Pb/$^{235}$U | | $^{206}$Pb/$^{238}$U | | $^{207}$Pb/$^{206}$Pb | | $^{207}$Pb/$^{235}$U | | $^{206}$Pb/$^{238}$U | |
|---|---|---|---|---|---|---|---|---|---|---|---|---|---|---|---|---|
| | (ppm) | | | | Ratio | 1σ | Ratio | 1σ | Ratio | 1σ | Age (Ma) | 1σ | Age (Ma) | 1σ | Age (Ma) | 1σ |
| Porphyric biotite syenogranite (AK-1) | | | | | | | | | | | | | | | | |
| 1 | 44.41 | 2238.8 | 402.3 | 0.18 | 0.0479 | 0.0017 | 0.1146 | 0.0046 | 0.0173 | 0.0002 | 94.5 | 91.7 | 110.2 | 4.2 | 110.7 | 1.4 |
| 2 | 17.28 | 826.0 | 429.8 | 0.52 | 0.0511 | 0.0035 | 0.1182 | 0.0083 | 0.0170 | 0.0004 | 242.7 | 157.4 | 113.4 | 7.5 | 108.6 | 2.4 |
| 3 | 8.07 | 346.8 | 330.6 | 0.95 | 0.0563 | 0.0042 | 0.1258 | 0.0102 | 0.0162 | 0.0004 | 464.9 | 166.6 | 120.3 | 9.2 | 103.8 | 2.7 |
| 4 | 62.38 | 2573.5 | 3812.5 | 1.48 | 0.0491 | 0.0017 | 0.1050 | 0.0038 | 0.0155 | 0.0003 | 153.8 | 76.8 | 101.4 | 3.5 | 99.5 | 1.7 |
| 5 | 14.24 | 683.5 | 424.5 | 0.62 | 0.0501 | 0.0044 | 0.1117 | 0.0102 | 0.0162 | 0.0003 | 198.2 | 192.6 | 107.5 | 9.3 | 103.3 | 1.8 |
| 6 | 7.91 | 355.2 | 249.2 | 0.70 | 0.0506 | 0.0039 | 0.1151 | 0.0081 | 0.0171 | 0.0004 | 233.4 | 181.5 | 110.6 | 7.4 | 109.3 | 2.7 |
| 7 | 14.36 | 704.6 | 323.1 | 0.46 | 0.0507 | 0.0038 | 0.1128 | 0.0082 | 0.0163 | 0.0003 | 233.4 | 174.1 | 108.6 | 7.5 | 104.4 | 1.6 |
| 8 | 17.60 | 813.6 | 470.0 | 0.58 | 0.0500 | 0.0037 | 0.1213 | 0.0096 | 0.0175 | 0.0004 | 194.5 | 176.8 | 116.3 | 8.7 | 112.0 | 2.3 |
| 9 | 16.44 | 877.5 | 173.0 | 0.20 | 0.0523 | 0.0039 | 0.1104 | 0.0066 | 0.0158 | 0.0004 | 298.2 | 168.5 | 106.3 | 6.0 | 100.8 | 2.3 |
| 10 | 31.80 | 1,672.7 | 410.3 | 0.25 | 0.0484 | 0.0022 | 0.1093 | 0.0051 | 0.0164 | 0.0002 | 116.8 | 105.5 | 105.3 | 4.6 | 104.9 | 1.4 |
| 11 | 16.05 | 563.0 | 942.1 | 1.67 | 0.0576 | 0.0045 | 0.1345 | 0.0112 | 0.0169 | 0.0004 | 522.3 | 172.2 | 128.2 | 10.0 | 108.1 | 2.3 |
| 12 | 34.50 | 1,689.3 | 291.9 | 0.17 | 0.0489 | 0.0019 | 0.1176 | 0.0048 | 0.0176 | 0.0003 | 142.7 | 88.0 | 112.9 | 4.4 | 112.2 | 1.9 |
| 13 | 10.53 | 527.8 | 233.5 | 0.44 | 0.0527 | 0.0046 | 0.1116 | 0.0099 | 0.0157 | 0.0003 | 322.3 | 201.8 | 107.4 | 9.1 | 100.3 | 2.2 |
| 14 | 15.19 | 670.7 | 274.1 | 0.41 | 0.0455 | 0.0037 | 0.1145 | 0.0098 | 0.0182 | 0.0003 | 205.2 | 185.1 | 110.0 | 8.9 | 116.3 | 2.0 |
| 15 | 134.67 | 7,111.0 | 727.3 | 0.10 | 0.0458 | 0.0014 | 0.1040 | 0.0032 | 0.0166 | 0.0002 | 117.0 | 105.8 | 100.5 | 2.9 | 105.9 | 1.3 |
| 16 | 14.43 | 571.6 | 274.4 | 0.48 | 0.0525 | 0.0035 | 0.1464 | 0.0091 | 0.0206 | 0.0004 | 305.6 | 151.8 | 138.7 | 8.0 | 131.4 | 2.8 |
| 17 | 14.96 | 731.3 | 344.8 | 0.47 | 0.0479 | 0.0039 | 0.1030 | 0.0078 | 0.0159 | 0.0003 | 100.1 | 172.2 | 99.5 | 7.2 | 101.5 | 1.8 |
| 18 | 16.97 | 726.2 | 394.8 | 0.54 | 0.0497 | 0.0031 | 0.1227 | 0.0072 | 0.0181 | 0.0003 | 189.0 | 144.4 | 117.5 | 6.5 | 115.7 | 1.9 |
| 19 | 20.19 | 863.9 | 564.2 | 0.65 | 0.0553 | 0.0032 | 0.1344 | 0.0079 | 0.0177 | 0.0003 | 433.4 | 125.0 | 128.1 | 7.0 | 113.0 | 2.0 |
| 20 | 34.46 | 1,694.8 | 506.2 | 0.30 | 0.0486 | 0.0018 | 0.1139 | 0.0042 | 0.0171 | 0.0002 | 127.9 | 87.0 | 109.5 | 3.8 | 109.2 | 1.6 |
| 21 | 11.36 | 500.8 | 236.9 | 0.47 | 0.0420 | 0.0028 | 0.1047 | 0.0069 | 0.0182 | 0.0004 | 205.1 | 184.9 | 101.1 | 6.3 | 116.3 | 2.3 |
| 22 | 31.41 | 1,318.6 | 1,488.9 | 1.13 | 0.0498 | 0.0022 | 0.1136 | 0.0050 | 0.0167 | 0.0002 | 187.1 | 103.7 | 109.3 | 4.6 | 106.5 | 1.5 |
| 23 | 17.78 | 917.0 | 228.8 | 0.25 | 0.0514 | 0.0028 | 0.1150 | 0.0062 | 0.0163 | 0.0002 | 261.2 | 130.5 | 110.6 | 5.7 | 104.1 | 1.5 |
| 24 | 9.47 | 376.2 | 285.7 | 0.76 | 0.0501 | 0.0044 | 0.1291 | 0.0120 | 0.0185 | 0.0004 | 211.2 | 183.3 | 123.3 | 10.8 | 118.3 | 2.3 |
| 25 | 11.62 | 486.1 | 325.0 | 0.67 | 0.0503 | 0.0042 | 0.1263 | 0.0105 | 0.0184 | 0.0003 | 205.6 | 185.2 | 120.8 | 9.5 | 117.3 | 2.1 |
| 26 | 45.82 | 2075.8 | 1,534.4 | 0.74 | 0.0516 | 0.0017 | 0.1169 | 0.0042 | 0.0164 | 0.0003 | 333.4 | 75.9 | 112.2 | 3.8 | 105.1 | 1.7 |
| 27 | 6.76 | 288.9 | 191.2 | 0.66 | 0.0508 | 0.0048 | 0.1174 | 0.0114 | 0.0173 | 0.0005 | 235.3 | 19.4 | 112.7 | 10.4 | 110.5 | 3.5 |
| 28 | 20.71 | 946.9 | 553.5 | 0.58 | 0.0437 | 0.0030 | 0.1036 | 0.0076 | 0.0172 | 0.0003 | 232.8 | 180.8 | 100.1 | 7.0 | 110.2 | 1.8 |
| 29 | 16.51 | 779.0 | 170.2 | 0.22 | 0.0481 | 0.0031 | 0.1194 | 0.0079 | 0.0180 | 0.0003 | 101.9 | 148.1 | 114.6 | 7.2 | 115.0 | 1.7 |
| 30 | 18.26 | 706.2 | 578.6 | 0.82 | 0.0548 | 0.0039 | 0.1395 | 0.0098 | 0.0186 | 0.0004 | 466.7 | 165.7 | 132.6 | 8.7 | 118.8 | 2.3 |
| 31 | 95.24 | 4994.2 | 496.7 | 0.10 | 0.0465 | 0.0012 | 0.1080 | 0.0031 | 0.0168 | 0.0002 | 33.4 | 50.0 | 104.1 | 2.9 | 107.5 | 1.5 |

form of scales and aggregate distribution, some of which are also strongly altered and sporadically distributed as pseudocrystal in the rocks (Figures 2G, I). In addition, there are still a small amount of muscovite (<3 vol%) in the rocks, which tend to be distributed in small scale-like aggregates around the biotite, and it should be considered secondary muscovite rather than primary muscovite (Figures 2G, I).

## 3 Analytical methods

In this study, t the rock samples of were systematically collected from the Late Mesozoic granitic pluton closely associated with copper and tin polymetallic ore bodies in the Akjilga mining area. These rock samples are relatively fresh and without obvious

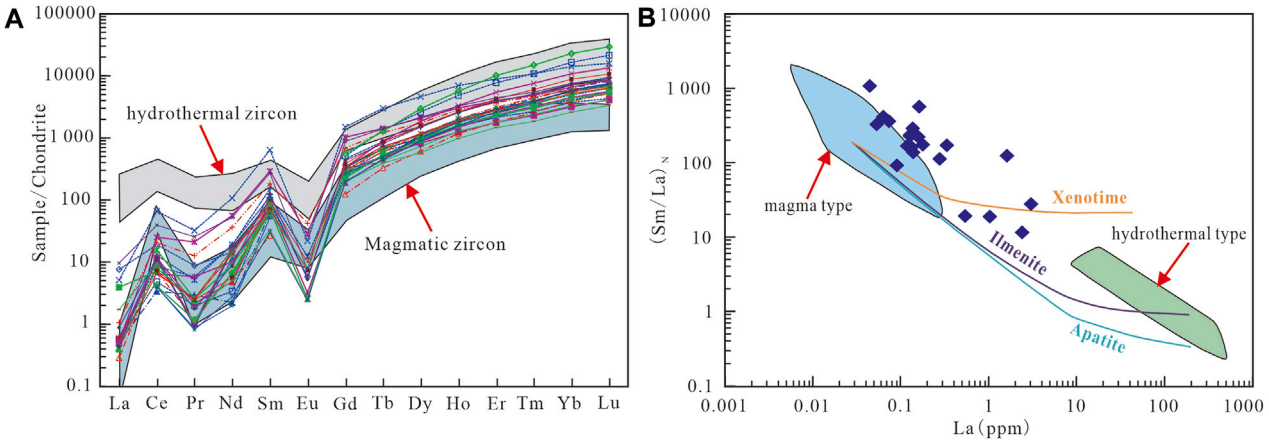


FIGURE 4
**(A)** Chondrite-normalized rare earth elements patterns of the zircons (normalization values from Boynton, 1984; distribution areas of magmatic and hydrothermal zircons according to Hoskin, 2005). **(B)** La vs. $(Sm/La)_N$ discrimination diagram between magmatic and hydrothermal zircons (after Hoskin, 2005).

alteration, mainly composed of alkaline feldspar, plagioclase, quartz and a small amount of biotite, as well as a very small amount of secondary muscovite, and the rock type is dominated by porphyric biotite syenogranite (Figures 2E–I). Based on detailed microscopic observations and identifications, seven samples were selected for the analysis of major, trace, and rare earth elements in the whole rock; one sample was selected for laser ablation–inductively coupled plasma–mass spectrometry (LA–ICP–MS) zircon U–Pb dating.

The zircon separation of porphyric biotite syenogranite (AK-1) was completed in Beijing GeoAnalysis CO., Ltd. Firstly, the fresh rock sample (~15 kg) collected in the field was mechanically crushed to obtain 60-mesh particles, and the zircon single minerals were separated by conventional gravity and electromagnetic methods. Thereafter, the zircon particles with good crystal shapes and high transparency were hand-selected using a binocular microscope. The selected zircon crystals were each fixed on an epoxy resin target with a diameter of 25 mm, and the zircon was polished until its central part was exposed. Finally, the polished zircon was analyzed by reflected light microscopy, transmitted light microscopy, and cathodoluminescence imaging to determine the internal structure of the zircon particles and ensure the suitability of the sample for LA–ICP–MS determination. The zircon U–Pb age and the content of trace elements were measured simultaneously by LA–ICP–MS (GeoLas 2005 and Agilent 7700a) at the Guangxi Key Laboratory of Concealed Metal Mineral Exploration, Guilin University of Technology. The working wavelength used in the laboratory was 193 nm. The laser denudation beam spot diameter was 32 μm, the denudation depth was 20–40 μm, and the pulse frequency was 6 Hz. Standard zircon GJ-1 and Plesovice zircon were used as external standard materials for the isotope calibration, and two standard samples were measured two times at intervals of eight analysis points. The trace-element content of zircon was calculated using NIST610 as the external standard and $^{29}Si$ as the internal standard (Liu et al., 2010). The detailed test process and principles have been provided elsewhere (Hou et al., 2009). The data processing of the zircon samples was performed using ICPMSDataCal 10.7 software (Liu et al., 2010). The calculation of the zircon U–Pb age-weighted average and the mapping of the harmonic map were completed using the Isoplot 3.0 program (Ludwig, 2003).

The contents of major, trace, and rare earth elements in the whole rock were determined at the laboratory of ALS Chemex (Guangzhou) Co., Ltd. First, the weathered skin of the rock sample was removed by a manual method and broken into fragments with a diameter of 1–10 mm using a crusher. Thereafter, the rock powder with under 200-mesh particles was ground in an agate mill machine and sent to the laboratory for analysis and testing. The elemental composition was determined by X-ray fluorescence analysis, and the analysis accuracy was better than 2%. Trace elements and REEs were analyzed and tested by inductively coupled plasma mass spectrometry (ICP–MS), where the analysis error of elements with content >10 ppm was less than 5%, and the analysis error of elements with contents <10 ppm was less than 10%.

# 4 Analytical result

## 4.1 LA–ICP–MS zircon U–Pb dating

The zircon particles in the porphyric biotite syenogranite sample (AK-1) are mostly colorless, with a few being light yellow. Most zircon crystals are idiomorphic, existing mainly in the form of semi-idiomorphic and idiomorphic short columns, with some existing in the form of long columns. Zircon particles are relatively granular and fine, with sizes (width) ranging from 30 to 90 μm, and their aspect ratios are between 1:1 and 4:1. Most of the zircon grains have noticeable oscillatory growth bands, indicating that they are typical magmatic zircons (Figure 3A). A total of 31 zircons were tested and analyzed from the porphyric biotite syenogranite sample (AK-1). The U–Pb age analysis data of the zircon are shown in Table 1. As shown in Table 1, the Th and U contents in zircon vary significantly (Th = 170.2–3812.5 ppm, U = 288.9–7,111.0 ppm). However, the corresponding Th/U ratios are ≥0.1 (Th/U = 0.10–1.67), consistent with the typical magmatic zircon characteristics (Hoskin and

10.3389/feart.2023.1289000

**TABLE 2 Major (wt%) and trace (ppm) element compositions of Late Mesozoic granites.**

| Sample no. | AK-1 | AK-2 | AK-3 | AK-4 | AK-5 | AK-6 | AK-7 |
|---|---|---|---|---|---|---|---|
| $SiO_2$ | 74.20 | 77.03 | 75.86 | 75.44 | 76.15 | 75.48 | 75.55 |
| $TiO_2$ | 0.14 | 0.07 | 0.05 | 0.03 | 0.08 | 0.01 | 0.09 |
| $Al_2O_3$ | 13.44 | 12.23 | 13.01 | 13.30 | 12.63 | 13.27 | 13.05 |
| $Fe_2O_3^t$ | 0.91 | 0.79 | 0.88 | 0.61 | 0.87 | 0.85 | 0.90 |
| CaO | 0.76 | 0.38 | 0.44 | 0.41 | 0.53 | 0.34 | 0.63 |
| MgO | 0.22 | 0.10 | 0.05 | 0.08 | 0.11 | 0.05 | 0.14 |
| MnO | 0.05 | 0.04 | 0.05 | 0.04 | 0.05 | 0.04 | 0.05 |
| $K_2O$ | 4.60 | 4.67 | 4.74 | 4.81 | 4.61 | 4.54 | 4.59 |
| $Na_2O$ | 3.49 | 2.94 | 3.36 | 3.47 | 3.07 | 3.29 | 3.21 |
| $P_2O_5$ | 0.10 | 0.07 | 0.06 | 0.10 | 0.09 | 0.11 | 0.08 |
| LOI | 1.21 | 1.05 | 1.01 | 0.65 | 0.84 | 1.15 | 0.85 |
| Total | 100.03 | 100.16 | 100.39 | 99.55 | 99.9 | 99.98 | 100.04 |
| A/CNK | 1.11 | 1.16 | 1.14 | 1.14 | 1.15 | 1.21 | 1.15 |
| σ | 2.10 | 1.70 | 2.00 | 2.11 | 1.78 | 1.89 | 1.87 |
| Sc | 3.5 | 3.2 | 12.5 | 2.4 | 3.7 | 1.9 | 3.7 |
| V | 8 | 3 | 1 | 1 | 3 | 1 | 4 |
| Cr | 10 | 31 | 14 | 11 | 11 | 9 | 24 |
| Co | 1.4 | 0.6 | 0.3 | 0.4 | 0.8 | 0.4 | 0.9 |
| Ni | 1.4 | 0.7 | 1.0 | 0.6 | 0.8 | 0.5 | 0.9 |
| Cu | 2.2 | 3.5 | 44.4 | 3.3 | 1.6 | 1.1 | 3.6 |
| Zn | 21 | 11 | 49 | 12 | 20 | 13 | 31 |
| Ga | 18.8 | 20.3 | 23.4 | 21.1 | 21.8 | 24.6 | 22.0 |
| Rb | 361 | 409 | 419 | 435 | 396 | 535 | 428 |
| Sr | 56.1 | 16.4 | 14.9 | 11.3 | 24.1 | 10.8 | 29.5 |
| Zr | 103 | 64 | 70 | 44 | 82 | 33 | 70 |
| Nb | 11.7 | 12.1 | 19.6 | 10.5 | 14.3 | 13.9 | 14.0 |
| Ta | 2.0 | 2.6 | 2.0 | 2.6 | 2.9 | 4.7 | 2.5 |
| Ba | 188.0 | 70.4 | 23.7 | 12.8 | 49.5 | 20.6 | 61.2 |
| Hf | 3.4 | 2.8 | 3.6 | 2.3 | 3.1 | 2.0 | 2.8 |
| Pb | 16 | 7.9 | 42.4 | 15.0 | 16.0 | 8.3 | 16.0 |
| Th | 15.05 | 13.65 | 14.75 | 9.81 | 12.95 | 11.25 | 15.40 |
| U | 4.44 | 10.55 | 5.21 | 16.90 | 11.70 | 38.60 | 6.68 |
| Cs | 7.46 | 7.59 | 11.20 | 10.35 | 7.83 | 7.16 | 10.30 |
| La | 20.3 | 13.0 | 12.4 | 5.7 | 11.6 | 3.1 | 15.3 |
| Ce | 43.4 | 30.1 | 32.3 | 13.5 | 26.8 | 8.2 | 34.4 |
| Pr | 4.81 | 3.55 | 3.75 | 1.60 | 3.24 | 1.06 | 3.92 |
| Nd | 16.7 | 12.9 | 14.8 | 6.1 | 12.4 | 4.2 | 15.5 |
| Sm | 3.94 | 3.42 | 4.53 | 1.71 | 3.25 | 1.50 | 3.99 |

(Continued on following page)

10.3389/feart.2023.1289000

**TABLE 2 (*Continued*) Major (wt%) and trace (ppm) element compositions of Late Mesozoic granites.**

| Sample no. | AK-1 | AK-2 | AK-3 | AK-4 | AK-5 | AK-6 | AK-7 |
|---|---|---|---|---|---|---|---|
| Eu | 0.33 | 0.08 | 0.08 | 0.03 | 0.14 | <0.03 | 0.15 |
| Gd | 3.56 | 3.42 | 5.34 | 2.16 | 3.09 | 1.45 | 3.59 |
| Tb | 0.63 | 0.72 | 1.09 | 0.49 | 0.65 | 0.35 | 0.72 |
| Dy | 3.83 | 4.83 | 6.90 | 3.23 | 4.47 | 2.42 | 4.67 |
| Ho | 0.84 | 1.12 | 1.57 | 0.72 | 1.05 | 0.51 | 1.07 |
| Er | 2.55 | 3.46 | 4.62 | 2.14 | 3.13 | 1.57 | 3.26 |
| Tm | 0.40 | 0.55 | 0.71 | 0.36 | 0.51 | 0.30 | 0.54 |
| Yb | 2.64 | 3.61 | 4.55 | 2.57 | 3.49 | 2.27 | 3.63 |
| Lu | 0.40 | 0.55 | 0.68 | 0.41 | 0.56 | 0.37 | 0.56 |
| Y | 23.4 | 29.1 | 40.3 | 19.2 | 29.0 | 14.8 | 31.4 |
| ∑REE | 104.33 | 81.31 | 93.32 | 40.72 | 74.38 | 27.33 | 91.30 |
| ∑LREE/∑HREE | 6.03 | 3.45 | 2.67 | 2.37 | 3.39 | 1.96 | 4.06 |
| δEu | 0.26 | 0.07 | 0.05 | 0.05 | 0.13 | 0.06 | 0.12 |
| $(La/Yb)_N$ | 5.52 | 2.58 | 1.95 | 1.59 | 2.38 | 0.98 | 3.02 |

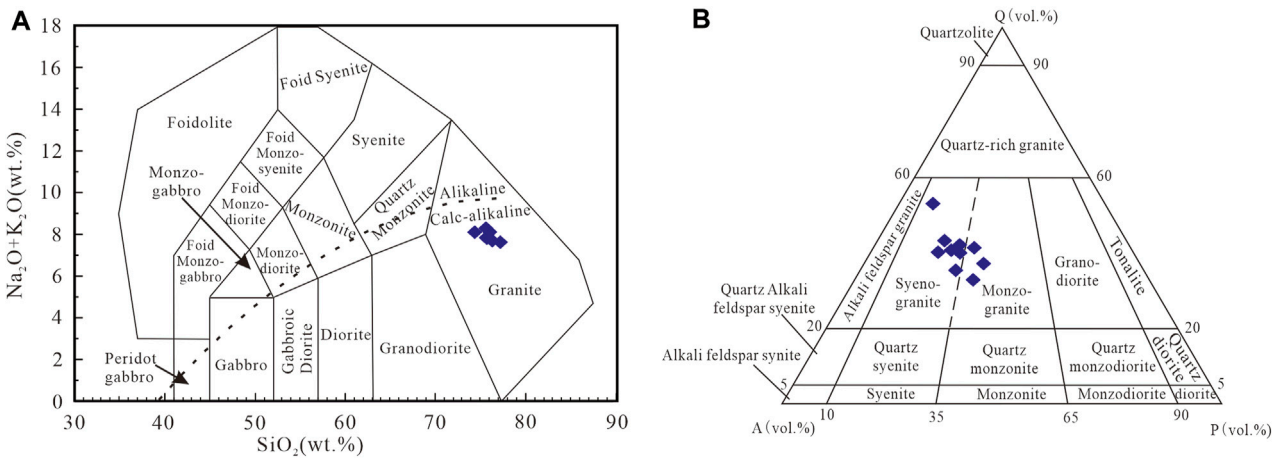


FIGURE 5
Geochemical discrimination diagrams for late Mesozoic granites: **(A)** $SiO_2$ vs. ($Na_2O+K_2O$) diagram (after Middlemost, 1994); **(B)** QAP diagram (after Streckeisen and Le Maitre, 1979).

Schaltegger, 2003). The standardized REE partitioning of zircon chondrites shows noticeable left-leaning patterns of light rare-earth element (LREE) deficit and heavy rare-earth element (HREE) enrichment, as well as noticeable positive Ce anomaly and negative Eu anomaly (Figure 4A). These are similar to the patterns observed for the REE model of "magmatic origin" zircon (Hoskin, 2005; Pelleter et al., 2007). The high $(Sm/La)_N$ ratio of zircon also indicates its magmatic origin (Figure 4B; Hoskin, 2005; Burnham, 2020). The $^{206}Pb/^{238}U$ surface ages of the 31 zircons range from 99.5 ± 1.7 Ma to 131.4 ± 2.8 Ma, and the zircon U-Pb age concordia diagram is all projected on or near the concordia line. Further, the age values of 30 of the measured sites form an age-concentration area on the concordia line. The weighted mean age is 108.3 ± 2.0 Ma (MSWD = 4.5, n = 30, Figure 3B). However, as shown in the dates of individual zircon grains (Figure 3C) and the probability density plot of the spot zircon ages (Figure 3D) for the porphyric biotite syenogranite (AK-1), the U-Pb ages exhibit sample-scale scatter. Molina et al. (2015) suggest that a large U–Pb zircon spot age dispersion at the sample scale does not necessary derive from analytical uncertainties, but may indicate a geological process of prolonged events of zircon crystallization. Therefore, the U-Pb ages of the porphyric biotite syenogranite in this area shows dispersion at the sample scale that may be due to a prolonged zircon crystallization.

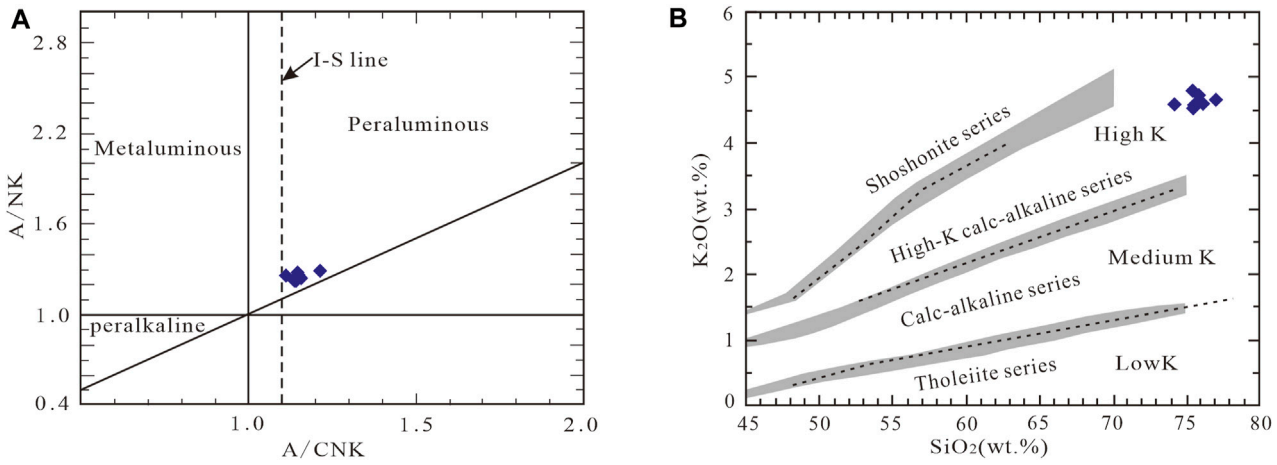


FIGURE 6
**(A)** A/CNK vs. A/NK diagram (after Maniar and Piccoli, 1989). **(B)** $SiO_2$ vs. $K_2O$ diagram (after Morrison, 1980).

## 4.2 Whole-rock major element compositions

The main-element analysis results of the Late Mesozoic granites in the Akjilga mining area are shown in Table 2. The table shows that the major elemental contents of the Late Mesozoic granites are comparable to the global average value of granites (Li et al., 1998). The $SiO_2$ (74.20–77.03 wt%) and total alkali ($K_2O$ + $Na_2O$ = 7.61–8.28 wt%, average value = 7.91 wt.%) contents are high, whereas the $Fe_2O_3T$ (1.21–1.82 wt.%), $TiO_2$ (0.01–0.14 wt.%), MgO (0.05–0.22 wt.%), CaO (0.34–0.76 wt.%), MnO (0.04–0.05 wt.%), and $P_2O_5$ (0.06–0.11 wt.%) contents are low. The content of $K_2O$ is significantly higher than that of $Na_2O$ ($K_2O/Na_2O$ = 1.32–1.59), indicating that the rocks are rich in silicon; high in potassium; and poor in iron, magnesium, calcium, sodium, titanium, and phosphorus. In the $SiO_2$–($Na_2O$ + $K_2O$) classification diagram (Figure 5A), the drop points of Late Mesozoic granite samples in this area all fall into the granite region. In the QAP classification diagram (Figure 5B), the drop points of the samples mainly fall into the syenogranite region and partly fall into the monzogranite area, indicating that the rock type is mainly syenogranite. The $Al_2O_3$ content of the rocks ranges from 12.23 to 13.44 wt.%, with an average value of 12.99 wt.%, and the aluminum saturation index (A/CNK) is 1.11–1.21 (average value = 1.15). In the A/CNK–A/NK diagram (Figure 6A), the input points of all the samples fall into the strong peraluminous granite region. In the $SiO_2$–$K_2O$ diagram (Figure 6B), the injection points of all the samples fall into the high-potassium calc-alkaline series region. According to the Harker diagram (Figure 7), there is a negative correlation between the $SiO_2$ content and the $Fe_2O_3^T$, MgO, $Al_2O_3$, $TiO_2$, CaO, MnO, $P_2O_5$, and total alkali ($K_2O$ + $Na_2O$) contents in the Late Mesozoic granite in the Akjilga mining area. It is suggested that feldspar, apatite, and titanium-rich minerals (such as ilmenite and titanium-magnetite) are involved in the separation and crystallization during the magmatic evolution. However, the contents of CaO and $Al_2O_3$ in the rock were significantly lower than those in the "continental crust" range, as determined by melting experiments. This indicates that in addition to crystallization separation, there may be mantle source materials involved in these magmas and a certain degree of crustal assimilation or mixing (Guo et al., 2012; Duan et al., 2015; Matínez Ardila et al., 2019).

## 4.3 Whole-rock trace and rare-earth element compositions

As shown in Table 2, the total content of REEs in the Late Mesozoic granite in the Akjilga mining area is relatively low, ranging from 27.33 ppm to 104.33 ppm, which is significantly lower than the total content of REEs in the global tin granite (∑REE = 134.6–368.0 ppm) (Zhao et al., 1990). The rocks all have strong negative Eu anomalies (δEu = 0.05–0.26); the ∑LREE/∑HREE ratio and the $(La/Yb)_N$ values are in the ranges of 1.96–6.03 and 0.98–5.52, respectively, and the degree of fractional distillation of heavy and heavy rare-earth elements is relatively low. However, from samples AK-4, AK-6→AK-2, AK-3→AK-1, AK-5, and AK-7, the total content of REEs and the related parameters regularly change. 1) The total content of rare earth increased from 27.33–40.72 ppm to 81.31–93.32 ppm to 74.38–104.33 ppm; 2) the ∑LREE/∑HREE ratio and the $(La/Yb)_N$ value also showed an increasing trend in general, the ∑LREE/∑HREE ratio and the $(La/Yb)_N$ value from 1.96 to 2.37 and 0.98 to 1.59→2.67 to 3.45 and 1.95 to 2.58→3.39 to 6.03 and 2.38 to 5.52, respectively. This indicates that the fractionation degree of LREEs and HREEs showed an increasing trend in general. 3) The standardized distribution patterns of REEs in chondrites all present as a strong "V" curve inclined to the right, the degree of which increases relatively (Figure 8A). The above results indicate that these rocks are genetically related and should be formed from homologous magma through crystallization differentiation.

As shown in Table 2, the Late Mesozoic granites in the Akjilga mining area are generally characterized by large ionic lithophile elements (LILEs, including Rb, Th, U, and K) and LREEs, as well as

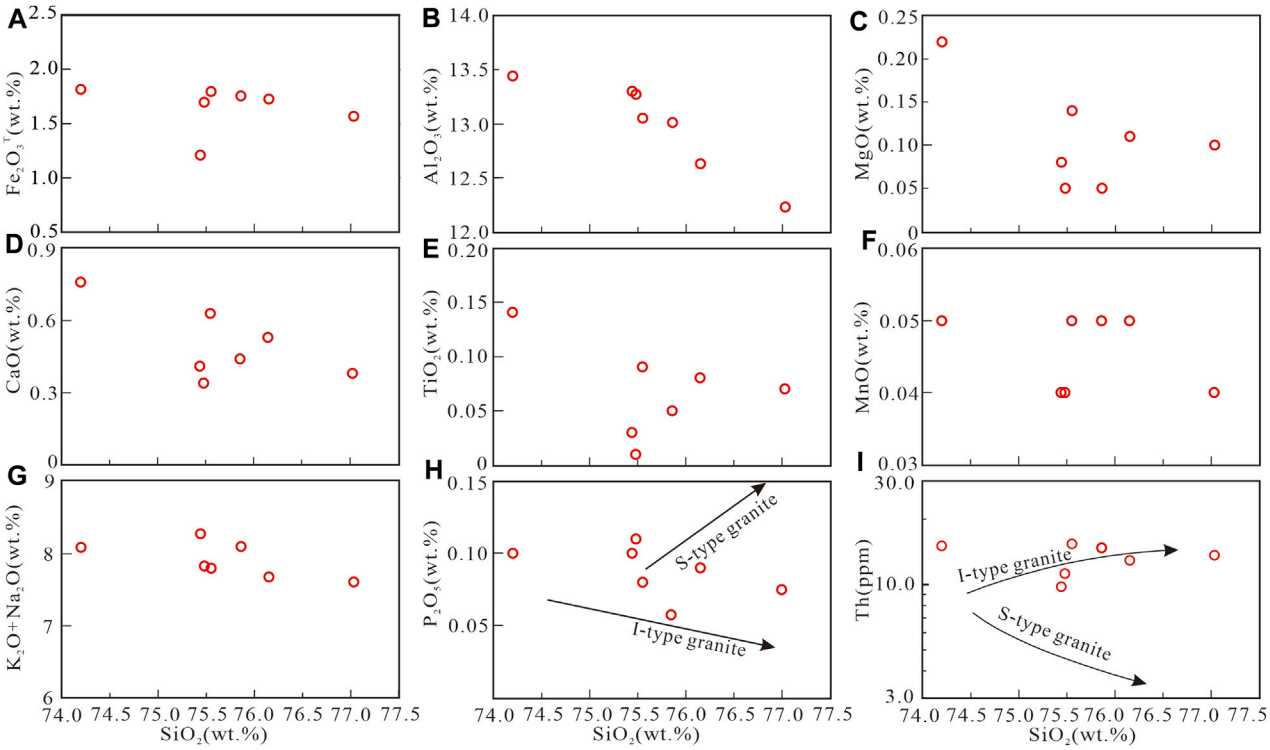


FIGURE 7
Harker diagrams of Late Mesozoic granites.

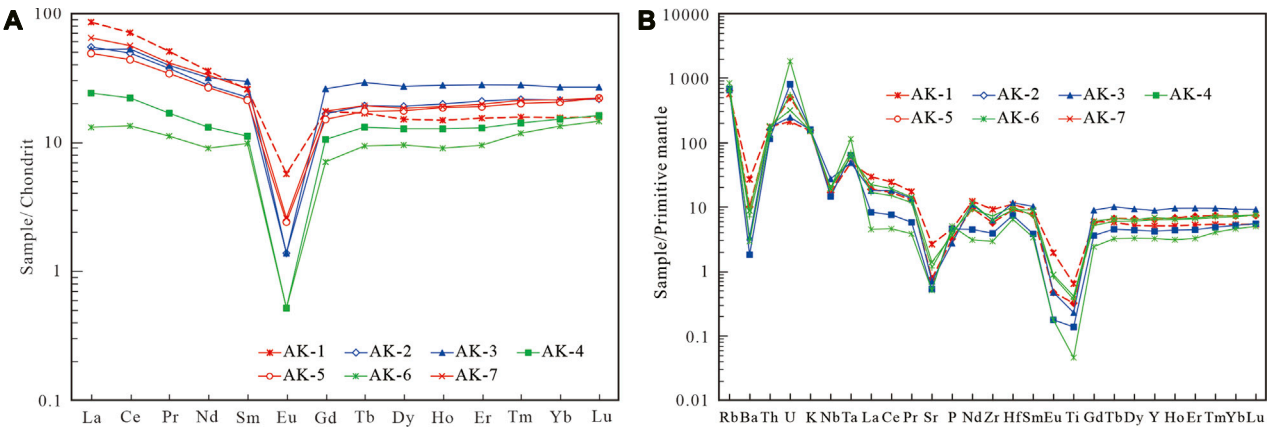


FIGURE 8
Chondrite-normalized REE patterns **(A)** and primitive mantle-normalized trace element spider diagrams **(B)** for Late Mesozoic granites. Chondrite- and primitive mantle-normalize values are from Sun et al. (1989).

relatively poor high-field-strength elements (HFSEs, including Nb, Sr, P, and Ti) and HREEs. Figure 8B shows a spider diagram of the normalized trace elements in the primitive mantle (Figure 8B). As shown, there are great similarities in the model curves of the Late Mesozoic granites in the Akjilga mining area. In addition to the P loss (valley value) of the AK-4 and AK-6 samples, the model curves of Ba, Nb, Sr–P, and Eu–Ti elements all negligible anomalies, whereas Rb, Th–K, and Ta elements all anomalies. This indicates that the magma may mainly originate from the crust or that there may be more shell source material in the source region (Wilson, 1989). In addition, Sr and Ba show relative deficit characteristics, indicating that the magma has undergone differentiation evolution.

# 5 Discussion

## 5.1 Formation age of the granite

Magmatic rocks are well developed in the South Pamir region of Tajikistan; however, the research on magmatic rocks is generally

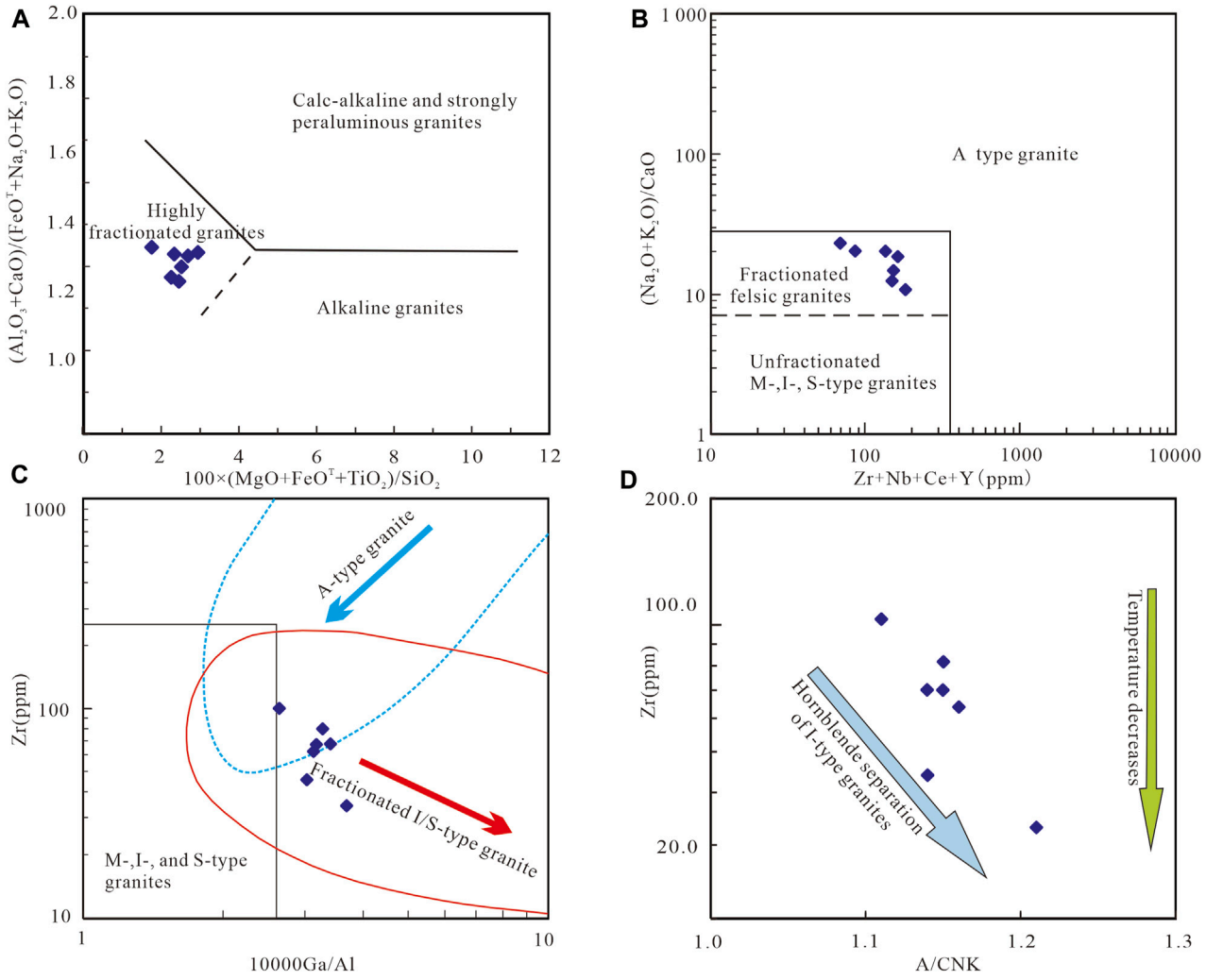


FIGURE 9
Genesis diagrams for late Mesozoic granites: **(A)** 100×(MgO + FeO + $TiO_2$)/$SiO_2$ vs. ($Al_2O_3$ + CaO)/(FeOT + $Na_2O$ + $K_2O$) diagram (after Sylvester, 1989); **(B)** (Zr + Nb + Ce + Y) vs. ($Na_2O$ + $K_2O$)/CaO diagram (after Whalen et al., 1987); **(C)** 10,000 Ga/Al vs. Zr diagram (after Whalen et al., 1987; the evolution trend line is after Wu et al., 2017); **(D)** Zr vs. A/CNK diagram (after Yuan et al., 2022).

limited because of the harsh natural geographical environment and inconvenient transportation system in this area. Some geologists often roughly divide the magmatic rocks in this area into two categories: pre-Cenozoic and Cenozoic rocks. The pre-Cenozoic magmatism mainly forms the huge South Pamir batholith dominated by granitic rocks. However, the Cenozoic magmatism forms only small granitic rocks, which distribute sporadically along the northern margin of the South Pamir block in the southern part of the Rushan–Pshart suture zone (Stübner et al., 2013a; b). Recently, some geologists discovered that the formation ages of granodiorite from the northern margin of the South Pamir block are 170 Ma and 198 Ma (Schwab et al., 2004; Chapman et al., 2018). The monzonite was formed at an age of 75 Ma (Schwab et al., 2004), and the age of the granite formation was 40 Ma (Volkov et al., 2016). This indicates that there are also Early Middle Jurassic and Late Cretaceous magmatism events, in addition to Eocene magmatism, on the northern margin of the South Pamir block. However, the research on the chronology of the large South Pamir batholith is limited. Some geologists studied the rocks around the batholith to the north and east of the South Pamir block, and they discovered that the formation ages of granodiorite and andesite are between 122 Ma and 103 Ma (Schwab et al., 2004; Stearns et al., 2015; Aminov et al., 2017; Chapman et al., 2018). However, the formation age of rocks in the central part of the batholith has rarely been reported in the published literature. In this study, the LA–ICP–MS zircon U–Pb weighted age of the porphyric biotite syenogranite, which is an important part of the South Pamir granite base in the Akjilga mining area, was 108.3 ± 2.0 Ma. This result indicates that it was formed in the Late Mesozoic (Early Cretaceous) period, which is basically consistent with the age values of rocks around the bedrock obtained by predecessors. However, it is worth noting that the U-Pb zircon point age of this sample exhibits significant dispersion at the sample scale, which may indicate that the geological process of zircon crystallization is a long-term process (Molina et al., 2015).

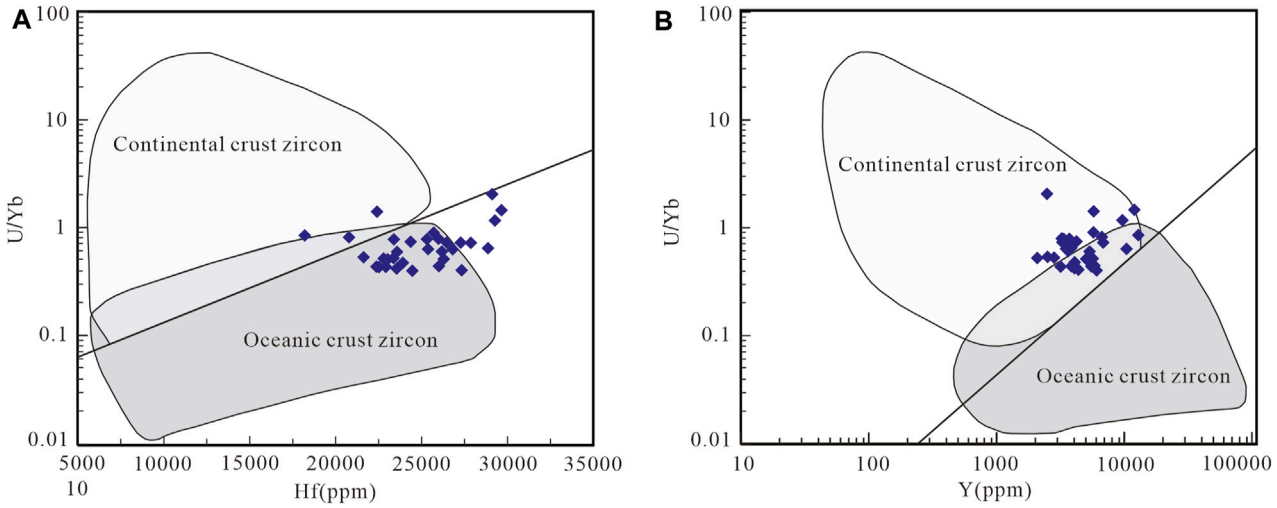


FIGURE 10
Diagrams of zircon from Late Mesozoic granites (modified after Grimes et al., 2007).

## 5.2 Petrogenesis and source of granitic magma

The results of the above geochemical characteristics show that the Late Mesozoic (Early Cretaceous) granites in the Akjilga mining area are mainly composed of porphyric biotite syenogranite. Compared with ordinary granite, these rocks have an unusually high $SiO_2$ content (74.20–77.03 wt%) and aluminum saturation index (A/CNK = 1.11–1.21), as well as very low $Fe_2O_3T$ (1.21–1.82 wt%) and $TiO_2$ (0.01–0.14 wt%), CaO (0.34–0.76 wt%), MgO (0.05–0.22 wt%), and $P_2O_5$ (0.06–0.11 wt%) contents. Thus, they are rich in silicon; high in potassium; and poor in iron, magnesium, calcium, sodium, titanium, and phosphorus. Further, they are classified as high-potassium calc-alkalinity strong peraluminous rocks. These porphyric biotite syenogranites exhibit high differentiation indexes (DI = 91.20–93.96); strong negative Eu anomaly; and significant losses of Ba, Nb, Sr, P, and Ti. In addition, the rocks have a low Zr content (33.0–103.0 ppm), and the ratios of Nb/Ta, Zr/Hf, Y/Ho, and ∑LREE/∑HREE are 2.96–9.80, 16.50–30.29, 25.67–29.35, and 1.96–6.03, respectively. The results show that these rocks experienced high differentiation and Late-stage melting-fluid interaction during magmatic evolution (Bau, 1996; Pérez-Soba and Villaseca, 2010; Ballouard et al., 2016; Wu et al., 2017). In the $100 \times (MgO + FeO + TiO_2)/SiO_2 - (Al_2O_3 + CaO)/(FeOT + Na_2O + K_2O)$ diagrams and the $(Zr + Nb + Ce + Y) - (Na_2O + K_2O)/CaO$ diagrams, the drop points of these rocks fall in the highly differentiated granite region (Figures 9A, B). This confirms the high differentiation of the granites (Wu et al., 2017). It is concluded that although the A-type granite is also highly differentiated, its characteristics are different from those of the highly differentiated I- or S-type granite. The former tends to be transformed from A-type granite into highly differentiated granite on the 10,000 × Ga/Al-Zr discriminant diagram. Contrarily, the 10,000 Ga/Al ratio of the I- or S-type granites gradually increases during the differentiation process. However, the 10,000 Ga/Al ratio of the porphyric biotite syenogranites in the Akjilga mining area tends to increase as the Zr content decreases (Figure 9C). Undoubtedly, the porphyric biotite syenogranites are highly differentiated I- or S-type granites, rather than the A-type granite. In addition, although the porphyric biotite syenogranite in this area is a strong peraluminous rock, which is similar to the S-type granite, it is notably different from the S-type granite in both petrography and geochemistry. 1) In terms of petrography, there are no aluminum-rich minerals (such as cordierite) unique to the S-type granite, although a small amount of hornblende (<2 vol%) and other landmark minerals of I-type granite are observed in some rocks. 2) In terms of the geochemical characteristics, the porphyric biotite syenogranites in this area all have a low $P_2O_5$ content, and their contents of main and trace elements (such as $P_2O_5$ and Th) change with the trend of $SiO_2$ (Figures 7H, I). Further, these rocks are significantly different from S-type granites and highly similar to I-type granites (Chappell and White, 1992; King et al., 1997). The A/CNK increases with the decrease in the Zr content (Figure 9D). This indicates that the crystallization of hornblende occurs separately in the process of magmatic evolution, which is also similar to the case with I-type granite (Clemens et al., 2011; Yuan et al., 2022). In addition, studies have shown that the existence of metamafic rock types with contemporaneous symbiosis is an important basis for identifying genetic types of highly differentiated granite (Wu et al., 2017). According to regional research data, besides monzonitic granite and granodiorite, the main rock types in the South Pamir batholith include contemporaneous diorite and gabbro (diabase); Early Cretaceous andesite with a thickness of thousands of meters; and small amounts of basalt, rhyolite, and epigenetic/ultraepigenetic porphyry (Schwab et al., 2004; Aminov et al., 2017; Chapman et al., 2018; Liu et al., 2020; Ma et al., 2022; Zhang et al., 2022). Based on the above petrographic and petrogeochemical characteristics, we tend to classify the highly evolved granites in the Akjilga mining area as highly differentiated I-type granites.

Usually, magmatic rocks from a single magma source area have relatively uniform Rb/Ti and La/Ce ratios (Marjorie, 1993), whereas

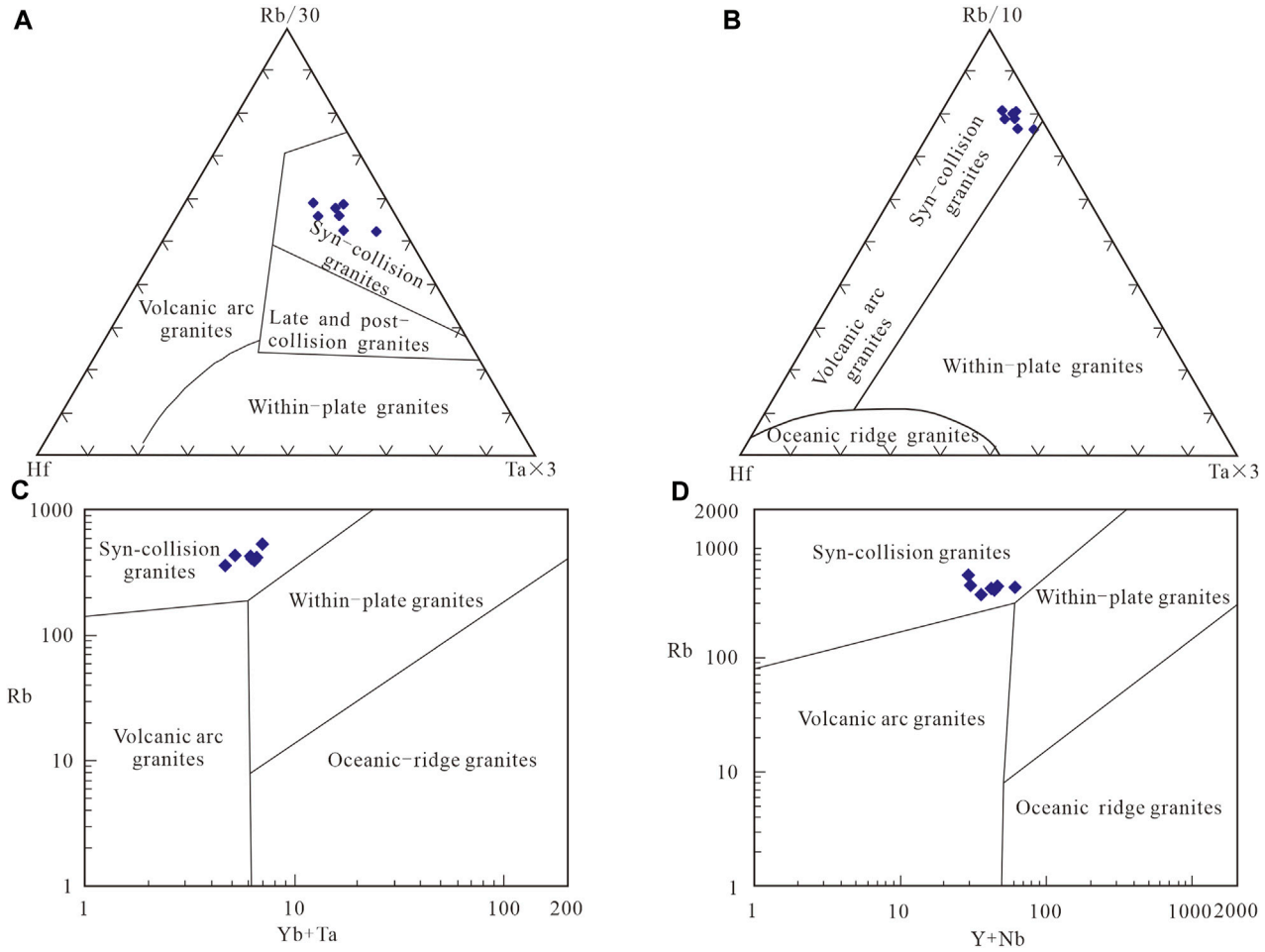


FIGURE 11
Discrimination diagrams illustrating tectonic setting of Late Mesozoic granites: **(A)** Rb/30 vs. Hf-Ta × 3 diagram (after Harris et al., 1986); **(B)** Rb/10 vs. Hf-Ta × 3 diagram (after Harris et al., 1986); **(C)** Rb vs. (Yb + Ta)diagram (after Pearce et al., 1984); **(D)** Rb vs. (Y + Nb)diagram (after Pearce et al., 1984).

the granites in the study area show variable Rb/Ti ratios (0.43–8.92) and La/Ce ratios (0.38–0.47), indicating that it has the characteristics of a mixed source area. The Zr/Nb (average 4.99), La/Nb (average 0.87), and Ba/Nb (average 4.80) ratios of the granites in the study area are significantly lower than the ratios of the continental crust (average 16.2, 2.2, and 54, respectively) and the primitive mantle (average 14.8, 0.94, and 9.0, respectively), and are close to the ratios of the EM II-enriched mantle (4.5-7.3, 0.89-1.09, and 7.3-13.3, respectively) (Saunders et al., 1988), further implying that the enriched lithospheric mantle is the primary source of parent magma of Late Mesozoic granites in the study area. As mentioned above, the contents of CaO and $Al_2O_3$ in the porphyric biotite syenogranite in this area were significantly lower than those in the "continental crust" range in the melting experiments. This indicates that these magmas have experienced fractional crystallization with only minor crustal assimilation or mixing, implying that these magmas are mainly mantle-derived (Guo et al., 2012; Qiu et al., 2014; Duan et al., 2015; Matínez Ardila et al., 2019). In addition, the trace-element composition of zircon can be used to distinguish continental crust zircon from oceanic crust zircon, which can help researchers effectively distinguish the magmatic origin environment and crystallization history of the host rock (Grimes et al., 2007; 2009). In the zircon-trace-element Hf–U/Yb and Y–U/Yb diagrams, the drop points of the porphyric biotite syenogranite (AK-1) zircons mainly fall in the overlapping area of oceanic and continental crust zircons or near the two sides of the dividing line (Figure 10). It is inferred that the recirculation of subducted ocean crust and the floor invasion of mantle-derived mafic magma played very important roles in the crustal growth in South Pamir.

The combination of the above features indicates that the Late Mesozoic granites in the study area are the products of homologous magma evolution, and the original magmas of these granites may have mainly derived from the enriched lithospheric mantle, which may be mafic magmas formed by the melting of the mantle wedge (subducted ocean crust replacement enrichment mantle). Subsequently, these mantle-derived mafic magmas assimilated or mixed with a small amount of crust-derived felsic magmas and underwent a highly differentiated evolution process of crystal differentiation, finally forming the Late Mesozoic (Early Cretaceous) highly differentiated I-type granite in the Akjilga mining area.

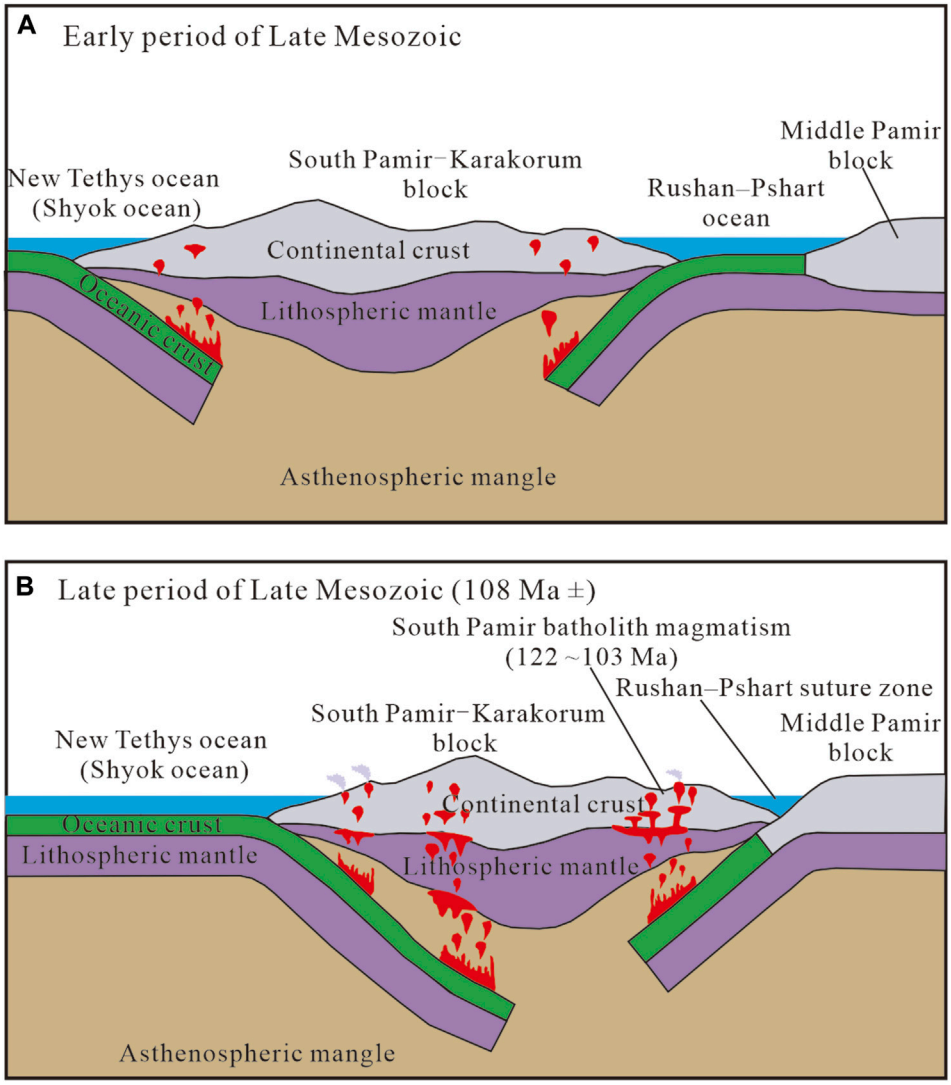


FIGURE 12
Geodynamic model for the Late Mesozoic magmatism in the South Pamir area, Tajikistan: **(A)** Early period of Late Mesozoic; **(B)** Late of Late Mesozoic (108 Ma ±).

## 5.3 Tectonic setting

As shown in the spiderweb of the normalized trace elements in the primitive mantle (Figure 8B), the Late Mesozoic granites in the Akjilga mine area feature abundant LILEs and LREEs; depleted HFSEs and HREEs; and significant negative anomalies of Nb, P, and Ti, similar to the elemental compositions of magmatic rocks found in subduction zones (Wilson, 1989). In various types of tectonic environment-discrimination diagrams (Figure 11), the drop points of the Late Mesozoic granites in the Akjilga mining area all fall in the syn-collisional granite region without exception, indicating that these granites were formed in the syn-collisional environment.

According to previous research data for the region, the Tanymas suture belt between the North Pamir block and the Middle Pamir block and the Rushan–Pshart suture belt between the Middle Pamir block and the South Pamir block are connected to the Jinshajiang suture belt and the Longmucuo–Shuanghu suture belt in China, respectively (Schwab et al., 2004; Liu et al., 2011; Robinson et al., 2012; Angiolini et al., 2013; Robinson, 2015). The Middle Pamir block and the South Pamir–Karakoram Block are connected to the Songpan–Ganzi Block and the Qiangtang Block in China, respectively (Zanchi et al., 2000; Ducea et al., 2003; Hacker et al., 2005; Robinson, 2015; Liu et al., 2020; Zhang et al., 2022). It is generally believed that the ocean basin represented by the Tanymas suture zone between the North Pamir block and the Middle Pamir block may have finally closed in the Late Triassic period (Dewey et al., 1988). However, the final closing time of the ocean basin represented by the Rushan–Pshart suture zone between the Middle Pamir block and the South Pamir block remains a controversial topic. Accordingly, the final closing time has been reported to be in the Late Triassic and Early Jurassic periods (Angiolini et al., 2013; Robinson, 2015), as well as in the Late Jurassic–Early Cretaceous period (Pashkov and Shvol'man, 1979; Schwab et al., 2004), two different perspectives. It is believed that with the bidirectional subduction of the ancient Tethys ocean, the central and South Pamir blocks converged with the North Pamir blocks successively, and the final merging time was approximately 180 Ma (Zhang et al., 2022). In addition, there were large-scale

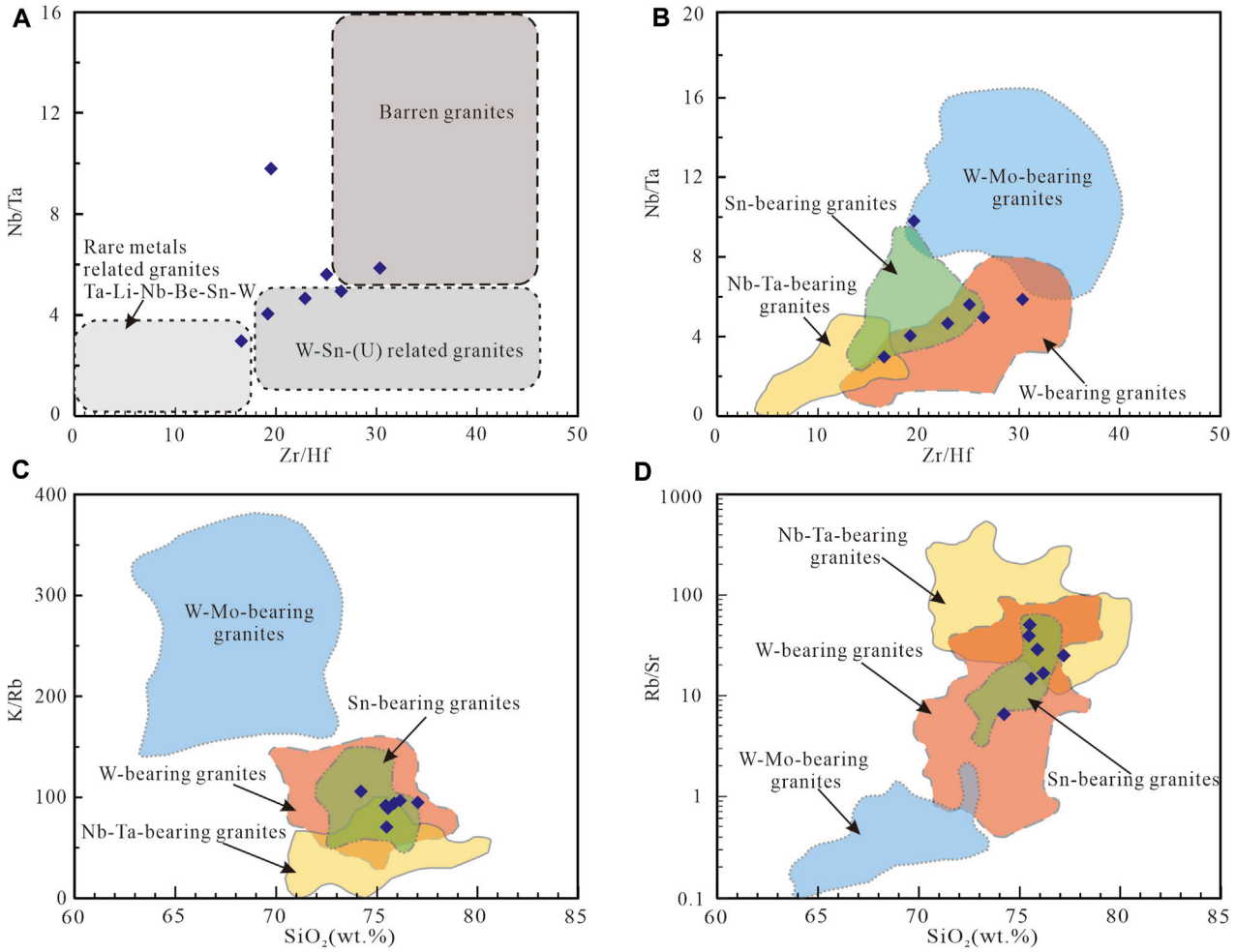


FIGURE 13
Discrimination diagrams illustrating Metallogenic relationship of Late Mesozoic granites: **(A)** Zr/Hf-Nb/Ta diagram (the color-shaded areas from Ballouard et al., 2016); **(B)** Zr/Hf-Nb/Ta diagram; **(C)** $SiO_2$-K/Rb diagram; **(D)** $SiO_2$-Rb/Sr diagram. The data of color-shaded areas of W-Mo, W, Sn, and Nb-Ta granites in the Jiangnan orogenic belt are quoted from Lu et al. (2022).

Cretaceous magmatic eruptions in the South Pamir–Karakoram–Qiangtang Block and the north of the South Pamir block, forming a magmatic belt with a width of >300 km (Chapman et al., 2018; Ma et al., 2022; Zhang et al., 2022). The age of magmatic activity in this magmatic belt is between 130 and 70 Ma, and the peak period is concentrated between 115 and 90 Ma (Schwab et al., 2004; Li et al., 2016; Aminov et al., 2017; Chapman et al., 2018; Liu et al., 2020; Ma et al., 2022; Zhang et al., 2022). Most geologists believe that these magmatic rocks may be Cretaceous island arc magmatic rocks formed by low-angle subduction to the north or the flat subduction of the New Tethys ocean between the Indian plate and the South Pamir–Karakoram Block (Faisal et al., 2016; Aminov et al., 2017; Chapman et al., 2018; Liu et al., 2020; Zhang et al., 2022).

The results of isotopic age testing and tectonic environment discrimination show that the formation age of the porphyric biotite syenogranite in the Akjilga mining area is 108.3 ± 2.0 Ma, and the tectonic environment is a syn-collisional environment. It is inferred that Late Mesozoic granites in the study area would have been formed immediately prior to collision, and it resulted in the subduction-collision of the Rushan-Pshart ocean between Middle Pamir block and the South Pamir block during the northward subduction process of the Late Mesozoic New Tethys ocean (Shyok ocean) (Figure 12). The Rushan–Pshart ocean between the South Pamir block and the Middle Pamir block not have been completely closed during early period of Late Mesozoic (Figure 12A); it was not until late period of Late Mesozoic (108 Ma ±) that the Middle Pamir block and the South Pamir block underwent subduction-collision, resulting in the assimilation or mixing of mafic magmas formed by the melting of the mantle wedge (subducted ocean crust replacement enrichment mantle) with a small amount of crust-derived felsic magmas, and underwent a highly differentiated evolution process of crystal differentiation, finally forming the Late Mesozoic (Early Cretaceous) highly differentiated I-type granites in the Akjilga mining area (Figure 12B).

## 5.4 Relationship between magmatism and mineralization

Previous studies have shown that highly differentiated granites often have noticeable metallogenic specificity, and the most thoroughly

differentiated end elements of such granites are called "rare metal or rare element granites" in mineral deposit circles. Their associated minerals include mainly W, Sn, Nb, Ta, Rb, Li, Be, and REEs, and magma is the main source region of the minerals. These minerals migrated and were enriched via magmatic-hydrothermal alteration (Wu et al., 2017; Zhao et al., 2022). The Late Mesozoic (Early Cretaceous) granites in the Akjilga mining area are considered highly differentiated granites. Detailed field geological investigation shows that the tin polymetallic ore bodies in the mining area are mainly produced in the skarn belt between the highly differentiated granites and the surrounding rocks in the Late Mesozoic (Early Cretaceous). Conversely, the dolomitic belt formed by magmatic-hydrothermal alteration features relatively high Rb, Nb, Ta, and other rare metal minerals. Further, the local rocks have reached the boundary grade or the lowest industrial grade in terms of rare metal minerals. In the diagram of Zr/Hf–Nb/Ta discrimination proposed by Ballouard et al. (2016) (Figure 13A), most of the points of porphyric biotite syenogranite in the Akjilga mining area fall in and near the W–Sn–(U) granite area, and one point falls in the rare metal granite area. The results show that the mineralization of Sn polymetals, as well as Rb, Nb, Ta, and other rare metals, in the Akjilga mining area is closely related to the intrusion of highly differentiated granite in the Early Cretaceous period in the area. However, the copper polymetallic ore bodies in the mine are mainly produced in the near north–south fault structure or jointed physical and chemical belt. Further, they noticeably cut the highly differentiated, Early Cretaceous granite area, indicating that the metallogenic age of the copper polymetallic deposit should be later than the Early Cretaceous period and that there is no direct genetic relationship with the intrusion of the highly differentiated Early Cretaceous granites. The Mesozoic granites in South China (Jiangnan Orogenic belt and Nanling area) also contain numerous highly differentiated genetic granites, and most of the large-scale tin (tungsten) and niobium–tantalum mineralizations in this area are related to the strongly evolved granites (particularly the highly differentiated granites) (Wu et al., 2017; Lu et al., 2022). In the Zr/Hf–Nb/Ta (Figure 13B), $SiO_2$–K/Rb (Figure 13C), and $SiO_2$–Rb/Sr (Figure 13D) diagrams, most of the sites of the porphyric biotite syenogranite in the Akjilga mining area fall in the overlapping area of W, Sn, and NB–Ta granites in the Jiangnan orogenic belt. This confirms that the intrusion of the highly differentiated Early Cretaceous granites in the Akjilga mining area is closely related to the Sn polymetallic mineralization and the mineralization of Nb, Ta, and other rare metals. Therefore, we believe that in addition to the great breakthrough in Sn polymetallic prospecting in recent years, the contact zone of high-differentiation granite in the Late Mesozoic (Early Cretaceous) period may also have good rare-metal prospecting potential.

## 6 Conclusion

Based on the study of lithography, geochemistry, and the zircon U–Pb chronology of Mesozoic granites in the Akjilga mining area, we draw the following conclusions.

(1) The Mesozoic granites in the Akjilga mining area are of two types: majorly porphyric biotite syenogranites and minorly porphyric biotite monzogranite. The LA–ICP–MS zircon U–Pb age of the porphyric biotite syenogranite was determined to be 108.3 ± 2.0Ma, which is a product of Early Cretaceous magmatic activity.

(2) The porphyric biotite syenogranite is rich in silicon; high in potassium; and poor in iron, magnesium, calcium, sodium, titanium, and phosphorus. The A/CNK values of the porphyric biotite syenogranites were determined to be 1.11–1.21, and they were classified as a high-potassium calc-alkali strong peraluminous rock. Trace-element analysis revealed the enrichment of LILEs and LREEs; the deficit of HFSEs and HREEs; and the significant negative anomalies of Nb, P, and Ti. Compared with ordinary granite, the porphyric biotite syenogranite shows a higher DI; a strong negative Eu anomaly, a low Zr content; and unusually low ratios of Nb/Ta, Zr/Hf, Y/Ho, and ∑LREE/∑HREE. The rocks have experienced a high degree of differentiation and strong melt-fluid interaction, and they are classified as highly differentiated I-type granite.

(3) The porphyric biotite syenogranite would have been formed immediately prior to collision, and it resulted in the subduction-collision of the Rushan-Pshart ocean between Middle Pamir block and the South Pamir block during the northward subduction process of the Late Mesozoic New Tethys ocean (Shyok ocean). At the same time, the mafic magmas formed by the melting of the mantle wedge (subducted ocean crust replacement enrichment mantle) was assimilated or mixed with a small amount of crust-derived felsic magmas, and underwent a highly differentiated evolution process of crystal differentiation, finally forming the Late Mesozoic granites in the Akjilga mining area.

(4) The intrusion of the porphyric biotite syenogranite in the Akjilga mining area is closely related to the mineralization of Sn polymetals as well as Nb, Ta, and other rare metals, and the contact zone of granite has good Sn polymetallic and rare-metal prospecting potentials.

## Data availability statement

The original contributions presented in the study are included in the article/Supplementary material, further inquiries can be directed to the corresponding author.

## Author contributions

D-RL: Writing–original draft. G-AH: Resources, Writing–review and editing. X-FQ: Funding acquisition, Methodology, Writing–review and editing. Y-LZ: Validation, Writing–review and editing. HM: Investigation, Writing–review and editing. W-LH: Software, Writing–review and editing.

## Funding

The author(s) declare financial support was received for the research, authorship, and/or publication of this article. This research was jointly supported by the National Natural Science Foundation of China (Approval number: 42162007) and the Geological Mineral Resources Survey and Evaluation Project of China Geological Survey (Approval number: DD20160124).

## Acknowledgments

We are grateful to our colleagues of Central Asia Minerals Co., Ltd for the help during the field geological survey. We also thank editors for their handling our paper, and two reviewers for their constructive comments that greatly improved our paper.

## Conflict of interest

Authors G-AH, HM, and W-LH were employed by Guangxi Nonferrous Metals Group Resources Exploration Co., Ltd.

The remaining authors declare that the research was conducted in the absence of any commercial or financial relationships that could be construed as a potential conflict of interest.

## Publisher's note



## Supplementary material

The Supplementary Material for this article can be found online at: https://www.frontiersin.org/articles/10.3389/feart.2023.1289000/full#supplementary-material

## References

Aminov, J., Ding, L., Mamadjonov, Y., Dupont-Nivet, G., Aminov, J., Zhang, L. Y., et al. (2017). Pamir Plateau formation and crustal thickening before the India-Asia collision inferred from dating and petrology of the 110-92 Ma Southern Pamir volcanic sequence. *Gondwana Res.* 51, 310–326. doi:10.1016/j.gr.2017.08.003

Angiolini, L., Zanchi, A., Zanchetta, S., Nicora, A., and Vezzoli, G. (2013). The cimmerian geopuzzle: New data from South Pamir. *Terra nova.* 25 (5), 352–360. doi:10.1111/ter.12042

Bai, L., Song, B. W., Li, G. H., Jiang, Y., and Sanjev, D. (2019). Seismic activity in the Himalayan orogenic belt and its related geohazards. *Adv. Earth Sci.* 34 (6), 629–639. doi:10.11867/j.issn.1001-8166.2019.06.0629

Ballouard, C., Poujol, M., Boulvais, P., Branquet, Y., Tartèse, R., and Vigneresse, J. L. (2016). Nb-Ta fractionation in peraluminous granites: a marker of the magmatic-hydrothermal transition. *Geology* 44 (3), 231–234. doi:10.1130/g37475.1

Bau, M. (1996). Controls on the fractionation of isovalent trace elements in magmatic and aqueous systems: evidence from Y/Ho, Zr/Hf, and lanthanide tetrad effect. *Contributions Mineralogy Petrology* 123, 323–333. doi:10.1007/s004100050159

Boynton, W. V. (1984). "Geochemistry of the rare earth elements: meteorite studies," in *Rare earth element geochemistry*. Editor P. Henderson (Amsterdam: Elservier), 63–114.

Burnham, A. D. (2020). Key concepts in interpreting the concentrations of the rare earth elements in zircon. *Chem. Geol.* 551, 119765. doi:10.1016/j.chemgeo.2020.119765

Burtman, V. S. (2000). Cenozoic crustal shortening between the Pamir and tien Shan and a reconstruction of the pamir–tien Shan transition zone for the cretaceous and palaeogene. *Tectonophysics* 319 (2), 69–92. doi:10.1016/s0040-1951(00)00022-6

Burtman, V. S., and Molnar, P. (1993). *Geological and geophysical evidence for deep subduction of continental crust beneath the Pamir*, 281. Boulder, Colorado, United States: Geological Society of America Special Paper, 1–76.

Cai, Z. H., Xu, Z. Q., Cao, H., and Liang, F. H. (2016). Exhumation of the Miocene mid-lower crust material in northeast Pamir: structural deformation and geochronological evidence from the west Kongur detachment. *Acta Geol. Sin.* 90 (11), 2999–3010. doi:10.3969/j.issn.0001-5717.2016.11.003

Cao, K., Mai, H. T., Wang, G. C., and Zhang, K. X. (2018). Mesozoic-Cenozoic tectonic and topographic development of the Pamir syntaxis and its potential effects on the sea retreat in the Tarim basin. *Quat. Sci.* 38 (1), 15–38. doi:10.3760/j.issn:0412-4030.2006.10.022

Cao, K., Wang, G. C., Bernet, M., Beek, P. V. D., and Zhang, K. X. (2015). Exhumation history of the West Kunlun mountains, northwestern tibet: evidence for a long-lived, rejuvenated orogen. *Earth Planet. Sci. Lett.* 432 (2015), 391–403. doi:10.1016/j.epsl.2015.10.033

Chapman, J. B., Scoggin, S. H., Kapp, P., Carrapa, B., Ducea, M. N., Worthington, J., et al. (2018). Mesozoic to cenozoic magmatic history of the Pamir. *Earth Planet. Sci. Lett.* 482, 181–192. doi:10.1016/j.epsl.2017.10.041

Chappell, B. W., and White, A. J. R. (1992). I- and S-type granites in the lachlan fold belt. *Earth Environ. Sci. Trans. R. Soc. Edinb.* 83 (1-2), 1–26. doi:10.1017/s0263593300007720

Cheng, J., Li, J. M., Zhang, Y. X., Li, Y. L., and Qin, F. (2022). Geological characteristics and the ore-forming process of the Dongduaoba—kuhe gold deposit in Tajikistan. *Mineral. Explor.* 13 (2-3), 247–257. doi:10.20008/j.kckc.202203010

Clemens, J. D., Stevens, G., and Farina, F. (2011). The enigmatic sources of I-type granites, the peritectic connexion. *Lithos* 126 (3-4), 174–181. doi:10.1016/j.lithos.2011.07.004

Dewey, J. F., Shackletonm, R. M., Chanmg, C. F., and Sun, Y. Y. (1988). The tectonic evolution of the Tibetan Plateau. *Philosophical Trans. R. Soc. Lond.* 327, 379–413. doi:10.1098/rsta.1988.0135

Duan, Z., Zhao, X. L., Xing, G. F., Yang, Z. L., Yu, M. G., Chen, Z. H., et al. (2015). Comparison study of petrogeneses and crust-mantle interactions between cretaceous lower and upper volcanic series in the adjacent area of zhejiang-fujian provinces. *Acta Geol. Sin.* 89 (2), 319–338. doi:10.19762/j.cnki.dizhixuebao.2015.02.009

Ducea, M. N., Lutkovm, V., Minaevm, V. T., Hacker, B., Ratschbacher, L., Luffi, P., et al. (2003). Building the Pamirs: the view from the underside. *Geology* 31, 849–852. doi:10.1130/g19707.1

Faisal, S., Larson, K. P., King, J., and Cottle, J. M. (2016). Rifting, subduction and collisional records from pluton petrogenesis and geochronology in the Hindu Kush, NW Pakistan. *Gondwana Res.* 35, 286–304. doi:10.1016/j.gr.2015.05.014

Fan, B. C., Meng, G. L., Liu, M. Y., Zhang, J., He, Z. X., Li, H. Y., et al. (2017). Division and features of the metallogenic units in Tajikistan. *Geol. Sci. Technol. Inf.* 36 (2), 168–175. doi:10.19509/j.cnki.dzkq.2017.0222

Fan, B. C., Zhang, J., Meng, G. L., Liu, M. Y., Li, H. Y., Абдумамадович, С., et al. (2020). Application of geochemical blocks theory in the prediction of gold resource potential in Tajikistan. *Northwest. Geol.* 53 (1), 138–145. doi:10.19751/j.cnki.61-1149/p.2020.01.012

Fan, B. C., Zhang, J., Meng, G. L., Xue, Z. K., Wu, H. H., Cao, J. F., et al. (2022). An assessment of lithium resource potentiality in Pamir syntax—based on 1:1 million scale of geochemical survey. *Northwest. Geol.* 55 (1), 156–166. doi:10.19751/j.cnki.61-1149/p.2020.01.012

Grimes, C. B., John, B. E., Cheadle, M. J., Mazdab, F. K., Wooden, J. L., Swapp, S., et al. (2009). On the occurrence, trace element geochemistry, and crystallization history of zircon from *in situ* ocean lithosphere. *Contributions Mineralogy Petrology* 158, 757–783. doi:10.1007/s00410-009-0409-2

Grimes, C. B., John, B. E., Kelemen, P. B., Mazdab, F. K., Wooden, J. L., Cheadle, M. J., et al. (2007). Trace element chemistry of zircons from oceanic crust: a method for distinguishing detrital zircon provenance. *Geology* 35 (7), 643–646. doi:10.1130/g23603a.1

Guo, F., Fan, W. M., Li, C. W., Zhao, L., Li, H. X., and Yang, J. H. (2012). Multi-stage crust-mantle interaction in SE China: temporal, thermal and compositional constraints from the Mesozoic felsic volcanic rocks in eastern Guangdong-Fujian provinces. *Lithos* 150, 62–84. doi:10.1016/j.lithos.2011.12.009

Hacker, B., Luffi, P., Lutkov, V., Minaev, V., Ratschbacher, L., Plank, T., et al. (2005). Near-ultrahigh pressure processing of continental crust: Miocene crustal xenoliths from the Pamir. *J. Petrology* 46, 1661–1687. doi:10.1093/petrology/egi030

Harris, N. B. W., Pearce, J. A., and Tindle, A. G. (1986). Geochemical characteristics of collision-zone magmatism. *Geol. Soc. Lond. Special Publ.* 19 (1), 67–81. doi:10.1144/gsl.sp.1986.019.01.04

Hoskin, P. W. O. (2005). Trace element composition of hydrothermal zircon and the alteration of Hadean zircon from the Jack Hills, Australia. *Geochimica Cosmochimica Acta* 69 (3), 637–648. doi:10.1016/j.gca.2004.07.006

Hoskin, P. W. O., and Schaltegger, U. (2003). The composition of zircon and igneous and metamorphic petrogenesis. *Rev. Mineralogy Geochem.* 53 (1), 27–62. doi:10.2113/0530027

Hou, K. J., Li, Y. H., and Tian, Y. Y. (2009). *In situ* U-Pb zircon dating using laser ablation-multi ion counting-ICP-MS. *Mineral. Deposits* 28 (4), 481–492. doi:10.1360/972008-2143

Imrecke, D. B., Robinson, A. C., Owen, L. A., Chen, J., Schoenbohm, L. M., Hedrick, K. A., et al. (2019). Mesozoic evolution of the eastern Pamir. *Lithosphere* 11, 560–580. doi:10.1130/l1017.1

King, P. L., White, A. J. R., Chappell, B. W., and Allen, C. M. (1997). Characterization and origin of aluminous A-type granites from the lachlan fold belt, southeastern Australia. *J. Petrology* 38 (3), 371–391. doi:10.1093/petroj/38.3.371

Li, B. Q., Meng, G. L., Qi, S. J., and Gao, P. (2013). *Introduction to geology and mineral resources of the Kush-West Kunlun metallogenic belt, Xingdu*. Beijing: Geological Publishing House, 1–163.

Li, J. M., and Zhou, K. F. (2019). The research of petrologygeochemistry and geochronology of ore-bearing granitic in Dongduaoba gold deposit, Tajikistan. *Acta Geol. Sin.* 93 (1), 197–214. doi:10.19762/j.cnki.dizhixuebao.2019011

Li, J. Y., Niu, Y. L., Hu, Y., Chen, S., Zhang, Y., Duan, M., et al. (2016). Origin of the late Early Cretaceous granodiorite and associated dioritic dikes in the Hongqilafu pluton, northwestern Tibetan Plateau: a case for crust–mantle interaction. *Lithos* 260, 300–314. doi:10.1016/j.lithos.2016.05.028

Li, T., Yuan, H. Y., and Wu, S. X. (1998). On the average chemical composition of granitoids in China and the World. *Geotect. Metallogenia* 22 (1), 24–29.

Liu, J., Tang, Y. H., Tang, G. M., and Tang, Z. X. (2021). Model of tin-copper ore formation and finding signs in the akjiga mining district, republic of Tajikistan. *China Metal. Bull.* (12), 75–76. doi:10.3969/j.issn.1672-1667.2021.12.038

Liu, X. Q., Zhang, C. L., Hao, X. S., Zou, H. B., Zhao, H. X., and Ye, X. T. (2020). Early cretaceous granitoids in the southern Pamir: implications for the meso-tethys evolution of the Pamir Plateau. *Lithos* 362-363, 105492. doi:10.1016/j.lithos.2020.105492

Liu, Y., Santosh, M., Zhao, Z. B., Niu, W. C., and Wang, G. H. (2011). Evidence forpalaeo-Tethyan oceanic subduction within central Qiangtang, northern Tibet. *Lithos* 127, 39–53. doi:10.1016/j.lithos.2011.07.023

Liu, Y. S., Gao, S., Hu, Z. C., Gao, C. G., Zong, K. Q., and Wang, D. B. (2010). Continental and oceanic crust recycling-induced melt-peridotite interactions in the trans-north China orogen: U-Pb dating, Hf isotopes and trace elements in zircons from mantle xenoliths. *J. Petrology* 51 (1-2), 537–571. doi:10.1093/petrology/egp082

Lu, J. J., Zhang, R. Q., Huang, X. D., Zhang, Q., Li, X. Y., Zhou, W. F., et al. (2022). Metallogenic characteristics of tungsten, tin, and rare metal deposits in the jiangnan orogenic belt. *South China Geol.* 38 (3), 359–381. doi:10.3969/j.issn.2097-0013.2022.03.001

Ludwig, K. R. (2003). *User's manual for Isoplot 3.0: a geochronological toolkit for microsoft excel*. Berkeley: Geochronology Center Special Publication, 1–70.

Ma, X., Dan, W., Wang, Q., Yang, Y. N., Tang, G. R., and Tang, G. J. (2022). Petrogenesis of the Taxkorgan early Cretaceous two-mica granites and medium-mafic magmatic enclaves in the central Pamir and their geological significance. *Geotect. Metallogenia* 46 (2), 380–397. doi:10.16539/j.ddgzyckx.2022.02.012

Malz, N., Pfänder, J. A., Ratschbacher, L., and Hacker, B. R. (2012). Cretaceous-cenozoic magmatism in the Pamir and a comparison with tibet. *J. Nepal Geol. Soc.* 45, 119–120.

Maniar, P. D., and Piccoli, P. M. (1989). Tectonic discrimination of granitoids. *Geol. Soc. Am. Bull.* 101 (5), 635–643. doi:10.1130/0016-7606(1989)101<0635:tdog>2.3.co;2

Marjorie, W. (1993). Magmalic differentilization. *J. Ceological Soc.* 150 (4), 611–624. doi:10.1144/gsjgs.150.4.0611

Martínez Ardila, A. M., Paterson, S. R., Memeti, V., Parada, M. A., and Molina, P. G. (2019). Mantle driven cretaceous flare-ups in Cordilleran arcs. *Lithos* 326-327, 19–27. doi:10.1016/j.lithos.2018.12.007

Middlemost, E. A. (1994). Naming materials in the magma/igneous rock system. *Earth Sci. Rev.* 37, 215–224. doi:10.1016/0012-8252(94)90029-9

Mo, H., Liu, T., Tang, Z. X., Deng, W. M., Ye, J. W., and Tang, Y. H. (2019). Metallogenic model and prospecting prediction of silver-copper mine in the Akjiga mining district of Gorno-Badakhshan autonomous oblast, republic of Tajikistan. *World Nonferrous Met.* 93 (6), 95. doi:10.3969/j.issn.1002-5065.2019.06.045

Molina, P. G., Parada, M. A., Gutiérrez, F. J., Ma, C. Q., Li, J. W., Liu, Y. Y., et al. (2015). Protracted late magmatic stage of the caleu pluton (central Chile) as a consequence of heat redistribution by diking: insights from zircon data and thermal modeling. *Lithos* 227, 255–268. doi:10.1016/j.lithos.2015.04.008

Morrison, G. W. (1980). Characteristics and tectonic setting of the shoshonite rock association. *Lithos* 13, 97–108. doi:10.1016/0024-4937(80)90067-5

Pashkov, B., and Shvol'man, V. (1979). Rift margins of Tethys in the pamirs. *Geotectonics* 13 (6), 447–456.

Pearce, J. A., Harris, N. B. W., and Tindle, A. G. (1984). Trace element discrimination diagrams for the tectonic interpretation of granitic rocks. *J. Petrology* 25, 956–983. doi:10.1093/petrology/25.4.956

Pelleter, E., Cheilletz, A., Gasquet, D., Mouttaqi, A., Annich, M., El Hakour, A., et al. (2007). Hydrothermal zircons: a tool for ion microprobe U-Pb dating of gold mineralization (Tamlalt-Menhouhou gold deposit-Morocco). *Chem. Geol.* 245 (3-4), 135–161. doi:10.1016/j.chemgeo.2007.07.026

Pérez-Soba, C., and Villaseca, C. (2010). Petrogenesis of highly fractionated I-type peraluminous granites: La Pedriza pluton (Spanish Central System). *Geol. Acta* 8 (2), 131–149. doi:10.1344/105.000001527

Qiu, L., Yan, D. P., Zhou, M. F., Arndt, N. T., Tang, S. L., and Qi, L. (2014). Geochronology and geochemistry of the Late Triassic Longtan pluton in South China: termination of the crustal melting and Indosinian orogenesis. *Int. J. Earth Sci.* 103 (3), 649–666. doi:10.1007/s00531-013-0996-z

Robinson, A. C. (2015). Mesozoic tectonics of the Gondwanan terranes of the Pamir plateau. *J. Asian Earth Sci.* 102, 170–179. doi:10.1016/j.jseaes.2014.09.012

Robinson, A. C., Ducea, M., and Lapen, T. J. (2012). Detrital zircon and isotopic constraints on the crustal architecture and tectonic evolution of the northeastern Pamir. *Tectonics* 31 (2), TC2016. doi:10.1029/2011tc003013

Robinson, A. C., Yin, A., Manning, C. E., Harrison, T. M., Zhang, S. H., and Wang, X. F. (2004). Tectonic evolution of the northeastern Pamir: constraints from the northern portion of the Cenozoic Kongur Shan extensional system, Western China. *Geol. Soc. Am. Bull.* 116 (7-8), 953–973. doi:10.1130/b25375.1

Robinson, A. C., Yin, A., Manning, C. E., Harrison, T. M., Zhang, S. H., and Wang, X. F. (2007). Cenozoic evolution of the eastern Pamir: implications for strain-accommodation mechanisms at the western end of the Himalayan-Tibetan orogen. *Geol. Soc. Am. Bull.* 119 (7-8), 882–896. doi:10.1130/b25981.1

Rutte, D., Ratschbacher, L., Khan, J., Stübner, K., Hacker, B. R., Stearns, M. A., et al. (2017b). Building the Pamir-Tibetan plateau-crustal stacking, extensional collapse, and lateral extrusion in the central Pamir: 2. Timing and rates. *Tectonics* 36 (3), 385–419. doi:10.1002/2016tc004294

Rutte, D., Ratschbacher, L., Schneider, S., Stübner, K., Stearns, M. A., Gulzar, M. A., et al. (2017a). Building the Pamir-Tibetan plateau-crustal stacking, extensional collapse, and lateral extrusion in the central Pamir: 1. Geometry and kinematics. *Tectonics* 36 (3), 342–384. doi:10.1002/2016tc004293

Saunders, A. D., Norry, M. J., and Tarney, J. (1988). Origin of MORB and chemically-depleted mantle reservoirs: trace element constraints. *J. Petrology, Special_Volume* Special_Volume (1), 415–445. doi:10.1093/petrology/special_volume.1.415

Schneider, F. M., Yuan, X., Schurr, B., Mechie, J., Sippl, C., Haberland, C., et al. (2013). Seismic imaging of subducting continental lower crust beneath the Pamir. *Earth Planet. Sci. Lett.* 375 (1), 101–112. doi:10.1016/j.epsl.2013.05.015

Schwab, M., Ratschbacher, L., Siebel, W., McWilliams, M., Minaev, V., Lutkov, V., et al. (2004). Assembly of the Pamirs: age and origin of magmatic belts from the southern Tien Shan to the southern Pamirs and their relation to Tibet. *Tectonics* 23, 1–31. doi:10.1029/2003tc001583

Sobel, E. R., Chen, J., Schoenbohm, L. M., Thiede, R. C., Stockli, D. F., Sudo, M., et al. (2013). Oceanic-style subduction controls Late Cenozoic deformation of the northern Pamir orogen. *Earth Planet. Sci. Lett.* 363 (2), 204–218. doi:10.1016/j.epsl.2012.12.009

Stearns, M. A., Hacker, B. R., Ratschbacher, L., Rutte, D., and Kylander-Clark, A. R. C. (2015). Titanite petrochronology of the Pamir gneiss domes: implications for middle to deep crust exhumation and titanite closure to Pb and Zr diffusion. *Tectonics* 34, 784–802. doi:10.1002/2014tc003774

Streckeisen, A. L., and Le Maitre, R. W. (1979). A Chemical approximation to the modal QAPF classification of the igneous rocks. *Neues Jahrb. fur Mineral. Abh.* 136, 169–206. doi:10.1017/CBO9780511535581.001

Stübner, K., Ratschbacher, L., Rutte, D., Stanek, K., Minaev, V., Wiesinger, M., et al. (2013a). The giant Shakhdara migmatitic gneiss dome, Pamir, India-Asia collision zone: 1. Geometry and kinematics. *Tectonics* 32 (4), 948–979. doi:10.1002/tect.20057

Stübner, K., Ratschbacher, L., Weise, C., Chow, J., Hofmann, J., Khan, J., et al. (2013b). The giant Shakhdara migmatitic gneiss dome, Pamir, India-Asia collision zone: 2. Timing of dome formation. *Tectonics* 32 (5), 1404–1431. doi:10.1002/tect.20059

Sui, Y. H. (2010). The main rock gold deposits in Tajikistan. *Xinjiang Geol.* 28 (1), 99–103.

Sui, Y. H. (2018). Geological study of Jilau stockwork type gold deposit, Tajikistan. *Mineral. Explor.* 9 (1), 165–172.

Sun, S. S., McDonough, W. F., Saunders, A. D., and Norry, M. J. (1989). "Chemical and isotopic systematics of oceanic basalts: implications for mantle composition and processes," in *Magmatism in the ocean basins* (London: Special Publication), 313–345.

Sylvester, P. J. (1989). Post-collisional alkaline granites. *J. Geol.* 97 (3), 261–280. doi:10.1086/629302

Tu, G. C. (1999). Preliminary study on central Asia metallogenic domains. *Geol. Sci.* 34 (4), 341–348.

Volkov, V. N., Shatagin, K. N., and Kramchaninov, A. Y. (2016). On the role of contamination and hybridism in formation of the composite Raumid pluton granites (Pamir Mnts.): results of Sm-Nd Isotope Study. *Dokl. Earth Sci.* 470, 981–984. doi:10.1134/s1028334x16090233

Wang, Q. S. (2016). Analysis of global lithium resources exploration and development, supply and demand situation. *China Min. Mag.* 25 (3), 11–24. doi:10.3969/j.issn.1004-4051.2016.03.003

Wang, Q. S., Teng, J. W., Chen, S., Wen, W., Zhang, Y. Q., and Xu, W. M. (2020). Deep structure beneath the western Himalayan syntaxis-Pamir and surroundings and tectonic implications. *Chin. J. Geophys.* 63 (8), 2970–2977. doi:10.6038/cjg2020O0035

Whalen, J. B., Currie, K. L., and Chappell, B. W. (1987). A-type granites: geochemical characteristics, discrimination and petrogenesis. *Contributions Mineralogy Petrology* 95 (4), 407–419. doi:10.1007/bf00402202

Wilson, M. B. (1989). *Igneous petrogenesis: a global tectonic approach*. London: Springer, 1–466.

Wu, F. Y., Liu, X. C., Ji, W. Q., Wang, J. M., and Yang, L. (2017). Highly fractionated granites: recognition and research. *Sci. China (Earth Sci.* 60 (7), 1201–1219. doi:10.1007/s11430-016-5139-1

Xiao, W. J., Windley, B. F., Hao, J., and Li, J. L. (2002). Arc-Ophiolite obduction in the western Kunlun range (China): implications for the palaeozoic evolution of central Asia. *J. Geol. Soc. Lond.* 159 (5), 517–528. doi:10.1144/0016-764901-093

Xue, C. J., Zhao, X. B., Mo, X. X., Chen, Y. C., Dong, L. H., Gu, X. X., et al. (2014a). Tectonic-metallogenic evolution and prospecting direction of giant gold-copper-lead-zinc metallogenic belt in western Tianshan. *J. Geol.* 88 (12), 2490–2531. doi:10.3969/j.issn.0001-5717.2014.12.025

Xue, C. J., Zhao, X. B., Mo, X. X., Dong, L. H., Gu, X. X., Bakhtiar, N., et al. (2014b). Asian gold belt in the western Tianshan and its geodynamics background, mineralization control and prospecting. *Earth Sci. Front.* 21 (5), 128–155. doi:10.13745/j.esf.2014.05.011

Yang, W. Z., Xue, C. J., Zhao, X. B., Zhao, S. M., Wei, J., Feng, B., et al. (2013). The discovery of the Kateba'asu large Au-Cu deposit in Xinyuan County, western Tianshan, Xinjiang. *Geol. Bull. China* 32 (10), 1613–1620. doi:10.3969/j.issn.1671-2552.2013.10.013

Yin, A., and Harrison, T. M. (2000). Geologic evolution of the Himalayan-Tibetan orogen. *Annu. Rev. Earth Planet. Sci.* 28 (1), 211–280. doi:10.1146/annurev.earth.28.1.211

Yuan, L. L., Wang, Y. F., Liu, J. P., Shao, Y. J., Liu, Z. F., Li, B., et al. (2022). Petro-geochemistry of Late Jurassic highly fractionated granites in the Xianghualing area of Hunan Province: constraints on petrogenesis and rare-metal mineralization. *Acta Petrol. Sin.* 38 (7), 2113–2138. doi:10.18654/1000-0569/2022.07.18

Zanchi, A., Poli, S., Fumagalli, P., and Gaetani, M. (2000). Mantle exhumation along the Tirich Mir fault zone, NW Pakistan: pre-mid-Cretaceous accretion of the Karakoram terrane to the Asian margin. *Geol. Soc.* 170 (1), 237–252. doi:10.1144/gsl.sp.2000.170.01.13

Zhang, C. L., Ma, H. D., and Liu, X. Q. (2022). Architecture and tectonic evolution of the Pamir Plateau: a review. *Geol. Rev.* 68 (5), 1653–1673. doi:10.16509/j.georeview.2022.08.015

Zhang, C. L., Zou, H. B., Ye, X. T., and Chen, X. Y. (2018). Tectonic evolution of the NE section of the Pamir Plateau: New evidence from field observations and zircon U-Pb geochronology. *Tectonophysics* 723, 27–40. doi:10.1016/j.tecto.2017.11.036

Zhang, G. Z., Li, Z. D., Dong, X. F., and Liu, J. Y. (2016a). Geological and S-Pb isotope tracing of Muruntau gold deposit in western Tianshan. *Acta Petrol. Sin.* 32 (5), 1333–1345.

Zhang, H. D., Lü, P. R., Luo, Y. J., Yang, B., Fan, B. C., and He, Z. X. (2019). Tectonic unit division of Pamir area in Tajikistan and its geological characteristics. *Geol. Explor.* 55 (1), 135–144.

Zhang, H. S., Hong, J., Zhang, H. D., Meng, G. L., Zhang, J., Liu, M. Y., et al. (2016b). The founding of Fe-Cu polymetallic mineralized bodies in Tuohetameishen. *Geol. Rev.* 62 (S1), 181–182. doi:10.16509/j.georeview.2016.s1.088

Zhao, P. L., Zajacz, Z., Tsay, A., and Yuan, S. D. (2022). Magmatic-hydrothermal tin deposits form in response to efficient tin extraction upon magma degassing. *Geochimica Cosmochimica Acta* 316, 331–346. doi:10.1016/j.gca.2021.09.011

Zhao, Y. M., Lin, W. W., and Bi, C. S. (1990). *Skarn deposits in China*. Beijing: Geological Publishing House, 232–256.